Physics of Plasmas

Tripolar guide magnetic fields due to island coalescence in solar wind current sheets: Simulation and theory

Cite as: Phys. Plasmas **29**, 112905 (2022); https://doi.org/10.1063/5.0102906
Submitted: 13 June 2022 • Accepted: 22 October 2022 • Published Online: 14 November 2022

David L. Newman, Stefan Eriksson and Giovanni Lapenta

Physics of Plasmas ARTICLE scitation.org/journal/php

Tripolar guide magnetic fields due to island coalescence in solar wind current sheets: Simulation and theory

Cite as: Phys. Plasmas **29**, 112905 (2022); doi: 10.1063/5.0102906
Submitted: 13 June 2022 · Accepted: 22 October 2022 ·
Published Online: 14 November 2022

David L. Newman,[1,a)] Stefan Eriksson,[2] and Giovanni Lapenta[3,b)]

AFFILIATIONS

[1]Center for Integrated Plasma Studies, University of Colorado, Boulder, Colorado 80309-0390, USA
[2]Laboratory for Atmospheric and Space Physics, University of Colorado, Boulder, Colorado 80303, USA
[3]Departement Wiskunde, Centrum voor Plasma-Astrofysica, Katholieke Universiteit Leuven, Celestijnenlaan 200B, 3001 Leuven, Belgium

[a)]**Author to whom correspondence should be addressed**: David.Newman@colorado.edu
[b)]**Also at**: Space Science Institute, Boulder, Colorado 80301, USA.

ABSTRACT

Reconnecting current sheets (CSs) in the solar wind near 1 AU have been previously identified that exhibit a modified Hall magnetic field perturbation of the nominal guide field characterized by a "tripolar" structure with depressions on both sides of a central maximum [Eriksson *et al.*, Astrophys. J. **805**, 43 (2015)]. Such CSs were inferred to contain multiple interacting islands based on measurements from all four Cluster satellites. A new set of 2D particle-in-cell simulations have been performed providing the foundation for a theoretical model for the origin of the tripolar guide-field perturbation. The simulations are initialized with a thin CS unstable to the formation of many small islands that undergo pairwise coalescence and growth. The guide field depressions develop as the result of a balance between the electrostatic (curl-free or irrotational) and electromagnetic (divergence-free or solenoidal) components of the parallel electric field. Field-line and flow-line tracing provide additional support for the model by demonstrating how a level of charge separation sufficient to support a large electrostatic potential can be maintained following island coalescence. A parameter study reveals that the plasma beta is the primary quantity controlling the evolution of the tripolar field. Dependence on the initial guide-field strength is also investigated.

I. INTRODUCTION

Current sheets (CSs) occur throughout the solar wind wherever the vector magnetic field $\mathbf{B}$ changes over a small distance such that the current, approximated by $\mathbf{J} \propto \nabla \times \mathbf{B}$, is localized to a narrow layer. While an isolated CS can be a fairly simple structure, turbulent regions may consist of a tangled superposition of CSs, as suggested by Borovsky (2008). A primary example of a CS in the solar wind is the heliospheric current sheet (HCS) (Smith, 2001) associated with boundaries between sectors of opposite magnetization on the solar surface. The HCS can develop substructure (Crooker *et al.*, 1996; Khabarova *et al.*, 2015), which is the subject of a recent multi-scale statistical analysis (Eriksson *et al.*, 2022).

In its simplest form, an idealized isolated CS can be treated as a plasma structure in which spatial variation is confined to one dimension. Such a CS can be associated with a *discontinuity* in the solar wind plasma, such as a tangential discontinuity (TD) or a rotational discontinuity (RD) (Tsurutani *et al.*, 2011 and references therein), although actual CSs are typically more complex. The primary difference between a TD and an RD is that the latter can have a component of $\mathbf{B}$ that is *normal* to the CS while a TD does not. It has been suggested (Artemyev *et al.*, 2019) that RDs evolve into TDs due to magnetic field line stretching.

A TD and its associated CS can be treated as an interface between two separate plasma regions with $\mathbf{B}_1$ and $\mathbf{B}_2$ being the respective magnetic field vectors on the two sides of the interface. Other plasma parameters (e.g., density and temperature) can also differ on the two sides. It is usual to use (L, M, N) coordinates to orient observed CSs, with N being normal to the plane forming the interface. For an ideal TD, M is defined as the direction normal to $\mathbf{B}_2 - \mathbf{B}_1$ and L completes the right-hand coordinate system. Thus, $B_{1M} = B_{2M}$, which is referred to as the *guide* field $B_g \hat{\mathbf{e}}_m$, while B_{1L} and B_{2L} point in opposite directions—although not necessarily equal in magnitude—and are referred

to jointly as the *reversing* magnetic field. These conditions, however, do not necessarily hold within the narrow width of the CS itself. In the special case where the plasma on the two sides of the CS is the same, except for the sign of B_L, the CS is referred to as being *symmetric*.

Closely related to the magnitude of B_g relative to the reversing B_L component is the magnetic *shear* angle $\Delta\theta = \cos^{-1}(\mathbf{B}_1 \cdot \mathbf{B}_2/|B_1||B_2|)$, which specifies the angle of rotation of **B** across the CS. This rotation angle lies in the range $0 < \Delta\theta \leq 180°$, with the maximum value associated with $B_g = 0$ and the low end of the range associated with guide fields much larger than the reversing field.

A subset of CSs are distinguished by the fact that they are undergoing magnetic reconnection somewhere along their length. This subset of CSs is particularly important because magnetic reconnection mediates the transfer of energy from magnetic fields to particles. In fact, the presence of accelerated ion *jets* in conjunction with a rotating magnetic field is a key identifying signature of a reconnecting CS (Gosling, 2012). However, not all CSs are equally likely to exhibit evidence of reconnection.

There is a significant difference between the distribution of shear angles for all CSs compared to the distribution for reconnecting CS, with the former (Malaspina *et al.*, 2013; Vasko *et al.*, 2021, 2022) favoring smaller values of $\Delta\theta$ relative to the latter (Gosling, 2012; Eriksson *et al.*, 2022). This difference is consistent with the identification (Borovsky and Denton, 2011) of CSs with $\Delta\theta > 45°$ as "strong." Electron heating is another signature of reconnection that has been associated with strong CSs (Zhou *et al.*, 2022). Strong heating can also be inferred from the partial variance of increments (PVI) and was found to be skewed toward large shear angles, with weaker heating identified for smaller shear angles (Chasapis *et al.*, 2015). Reconnecting CSs with a very small shear angle have, nevertheless, been observed in the solar wind (Gosling and Phan, 2013).

Another observable signature of a reconnecting CS is the presence of a perturbation to the guide field B_M. In the case of reconnection about a single isolated X-line, this perturbation, which is known as the Hall magnetic field, has quadrupolar symmetry about the X-line when $B_g = 0$—a configuration referred to as *antiparallel* reconnection. This symmetric Hall-field pattern becomes distorted in the presence of a guide field (Ricci *et al.*, 2004).

Reconnection exhausts observed in conjunction with a *tripolar* guide-field perturbation have been reported using data from the ARTEMIS and WIND missions (Eriksson *et al.*, 2014) and from the four-satellite Cluster mission (Eriksson *et al.*, 2015). This tripolar signature consists of an enhancement of B_M bordered by depressions on both sides of the central maximum. Such a tripolar signature is inconsistent with the quadrupolar Hall field predicted for reconnection near a single X-line, with or without a background guide field. Eriksson *et al.* (2014) proposed an interpretation of the tripolar B_M perturbation as resulting from the satellites crossing obliquely between two X-lines so that the two negative depressions in B_M were due to the negative branches of the quadrupolar Hall field coming, respectively, from each of the neighboring X-lines—taking into account the Hall-field asymmetry due to the background guide field.

Subsequently, Eriksson *et al.* (2015) used the spatially separated trajectories of the four Cluster satellites to infer the existence of interacting magnetic islands in the vicinity of the observed tripolar B_M. This interpretation was supported by the results of 2D particle-in-cell (PIC) simulations showing enhanced negative B_M perturbations above and below merging or coalescing islands. These simulations also revealed the presence of a region near the magnetic separatrices associated with pairs of interacting islands in which the direction of the current, when projected into the simulation plane, is opposite to the direction near the center of the islands. This layer of reversed current, which is predominantly due to electrons, was shown to be closely associated with the B_M reversals. We note that the tripolar B_M signature was not observed in simulations containing multiple islands *not* undergoing coalescence (Huang *et al.*, 2012), which instead exhibited a dip in B_M in the center of the islands. This difference also points to the role played by island coalescence in the formation of the B_M reversals.

While previous 2D PIC simulations have verified the connection between the structure of the current near the separatrix and the reversals of the out-of-plane B_M field associated with the observed tripolar structure, it could not be determined *why* these features develop and how they are causally connected. The primary focus of the present study is, therefore, to identify the underlying mechanisms that lead to the formation of the tripolar B_M structure in the vicinity of coalescing islands. Given the range of parameters that characterize reconnecting CSs in the solar wind, only a limited region of this parameter space can be simulated. We, therefore, consider primarily the single shear angle in our new simulation of $\Delta\theta = 90°$ ($B_g/B_L = 1.0$), which is intermediate between the values observed in Eriksson *et al.* (2014) with $\Delta\theta = 127°$ ($B_g/B_L = 0.5$) and Eriksson *et al.* (2015) with $\Delta\theta = 28.2°$ ($B_g/B_L = 3.9$), and only slightly higher than the median of $\Delta\theta = 67.5°$ from Eriksson *et al.* (2022). Guide field dependence will, however, be addressed briefly in Sec. IV C.

Our simulations also assume initial symmetry with all parameters, except for the orientation of **B**, being the same on both sides of the CS. They also start with equal ion and electron temperatures. As shown in Sec. III A, the evolution of a tripolar guide-field perturbation is governed largely by the ion plasma beta (the ratio of thermal to magnetic pressure). Since we initially assume that $T_e = T_i$, the total plasma beta is $\beta = \beta_i + \beta_e = 2\beta_i$. Observed CSs are generally asymmetric in that β is *not* the same on the two sides of the CS, with implications for the initiation of reconnection.

Recently, Eriksson *et al.* (2022) performed a 10-yr survey of CSs associated with reconnection exhausts in the solar wind using the Wind spacecraft (e.g., Wilson III *et al.*, 2021) at 1 AU. They confirmed a total of 3011 exhaust-associated CSs for which both ion and electron β values were available. Of these cases, 2600 or 86% were observed with local changes of $\Delta\beta = |\beta_2 - \beta_1|$ and magnetic field rotation angles $\Delta\theta$ such that $\Delta\beta < 2(L/d_i)\tan(\Delta\theta/2)$ for $L \leq 1d_i$. Here, β_1 and β_2 are the average *total* β values on the leading and trailing edges of the CSs, respectively, while $\Delta\theta = \cos^{-1}(\hat{\mathbf{B}}_1 \cdot \hat{\mathbf{B}}_2)$ from the time averaged magnetic fields at the leading ($\mathbf{B}_1$) and trailing ($\mathbf{B}_2$) edges of the same CSs. This condition for $\Delta\beta$ and $\Delta\theta$ is required to prevent a pressure-driven diamagnetic drift of the X-line along the CS, thereby allowing a reconnection process to proceed for asymmetric conditions of plasma pressure and magnetic field pressure (Swisdak *et al.*, 2003, 2010). Eriksson *et al.* (2022) assumed that similar values of $\Delta\beta$ and $\Delta\theta$ could have been present near the remote X-lines to suggest a median $L \sim 0.22d_i$ current sheet thickness based on all 2600 exhaust events. In other words, 50% of the 2600 cases were possibly associated with very thin $L < 0.22d_i$ CSs in the vicinity of the X-lines to allow reconnection onset, while the

other 50% of the 2600 exhausts were possibly associated with somewhat wider CS widths $0.22d_i < L < 1d_i$.

Another factor that can limit how thin a CS can be at the onset of reconnection is dynamical in origin (Loureiro and Uzdensky, 2015; Uzdensky and Loureiro, 2016). Consider a scenario where a discontinuity forms through the thinning of the interface between two plasmas, which takes the form of a Sweet–Parker CS (Sweet, 1958; Parker, 1957). As the CS thins, it will cross the threshold for the formation of plasmoid chains (Loureiro and Uzdensky, 2015). Once the plasmoid chains form and start to grow, the thinning of the CS terminates when averaged over the scale of many plasmoids. Therefore, the plasmoid-chain threshold thickness serves as a rough lower bound on the CS thickness.

The initial formation of a plasmoid chain from a thin Sweet–Parker CS provides the initial step in the development of a tripolar B_M perturbation as the individual plasmoids or magnetic islands begin to merge with one another. Although there have been many studies of interacting magnetic islands, the existence of tripolar B_M perturbations has not been discussed in the context of coalescing islands, to the best of our knowledge, with the exception of Eriksson *et al.* (2014, 2015).

Previous simulation studies of island coalescence have frequently focused on the process of electron acceleration in a turbulent setting (Zank *et al.*, 2014, 2015) or in the absence of a guide field (Oka *et al.*, 2010). While the presence of turbulence does not necessarily preclude the development of a tripolar B_M perturbation, identification of such a signature would likely be difficult. However, tripolar B_M perturbations do not form for an initially weak or zero guide field (see Sec. IV C). Plasma energization was also the focus of a simulation study of an isolated pair of islands with a strong guide field (Du *et al.*, 2018). Akhavan-Tafti *et al.* (2020) studied multiple X-line reconnection using the Vlasiator hybrid-Vlasov code and found the area occupied by coalescing islands was as likely to expand as contract but did not address guide-field perturbations. 3D simulations (Sauppe and Daughton, 2018) provide insight into laboratory experiments of merging flux ropes (Furno *et al.*, 2005).

The process by which pairs of islands in a plasmoid chain coalesce is necessarily indirect because particles—both electrons and ions—in the interior of the islands cannot easily penetrate the magnetic separatrix layer that separates the islands from the exterior plasma. However, the negative B_M perturbations responsible for the tripolar structure are typically outside the separatrix layer. The fact that the B_M reversals are remote from the particles within the merging islands is a strong indication that the generation mechanism must be mediated by the electromagnetic (EM) field, which, unlike the particles, is not impeded by the separatrix layer. The goal of this paper is, therefore, to describe a physical mechanism whereby coalescing islands drive the B_M reversals. As will be shown, the negative B_M perturbations arise due to a balance that develops between the *electrostatic* (ES) (curl-free) part of the electric field $\mathbf{E}$ and the *electromagnetic* (divergence-free) part of $\mathbf{E}$. The former is a consequence of local charge separation driven by island coalescence, while the latter, in turn, drives the magnetic perturbations via Faraday's law.

The remaining of this paper is structured as follows: Sec. II describes the theoretical and simulation methodology employed in this study. Section III contains the results of the simulations, including a parameter study showing β_i to be the fundamental determinant of how the tripolar B_M perturbation develops. This section also considers in detail various field and particle diagnostics for a single parameter set chosen to best illustrate the proposed source mechanism for the tripolar B_M perturbation. The discussion in Sec. IV provides a physical interpretation of the inferred source mechanism aided by diagnostics based on inferred particle orbits as presented in Appendix A. This section also briefly explores the dependence of the proposed model on the initial guide field, or equivalently, magnetic shear angle. Conclusions are presented in Sec. V.

II. THEORETICAL AND NUMERICAL MODEL

A. Fundamental equations and normalizations

All simulations are performed using the implicit moment particle-in-cell (PIC) method (Brackbill and Forslund, 1982; Lapenta *et al.*, 2006) implemented in the code iPic3D (Markidis *et al.*, 2010; Lapenta, 2012), which solves Maxwell's equations using as source terms the densities and currents accumulated on a grid from the spatial distribution of particle positions and velocities. The particle positions and velocities are, in turn, advanced via Newtonian mechanics subject to the electric and magnetic (i.e., Lorentz) forces. In terms of the (L, M, N) coordinates of Sec. I, the simulation coordinates (x, y) have the following associations: $L \rightarrow x$ and $N \rightarrow -y$ with the out-of-plane direction being $M \rightarrow z$. The minus sign on y is imposed so that both (L, M, N) and (x, y, z) are right handed. Because the iPic3D code uses a Gaussian (rather than SI) representation of Maxwell's equations, we likewise use the Gaussian form in this study. We present here for later reference the governing Maxwell equations

$$-\nabla^2\phi = \nabla\cdot\mathbf{E} = 4\pi\rho \quad \text{[Poisson]}, \tag{1}$$

$$\nabla\times\mathbf{B} = \frac{1}{c}\frac{\partial\mathbf{E}}{\partial t} + \frac{4\pi}{c}\mathbf{J} \quad \text{[Ampere]}, \tag{2}$$

and

$$\nabla\times\mathbf{E} = -\frac{1}{c}\frac{\partial\mathbf{B}}{\partial t} \quad \text{[Faraday]}. \tag{3}$$

In the simulation, distance is normalized to the ion inertial length $d_{i0} = c/\omega_{pi0}$ and time is normalized to the inverse plasma frequency ω_{pi0}^{-1}, where $\omega_{pi0} = (4\pi n_0 e^2/m_i)^{1/2}$. Here, n_0 is the *nominal* density. It immediately follows that velocities are normalized to the speed of light c. The implicit iPic3D algorithm remains numerically stable even when the time step Δt and grid spacing Δx is unable to resolve waves, such as electron plasma (Langmuir) oscillations with frequencies $f > 1/\Delta t$ or wavelengths $\lambda < \Delta x$. Within the simulation, all of the relevant quantities are dimensionless (designated by a tilde here) and relate to their physical counterparts for quantity A as follows: $A = [A]_0\tilde{A}$. Thus, square brackets with subscript zero designate the conversion factor from code to physical units. All conversion factors can be built up from the most fundamental ones (velocity and density) using the aforementioned scale factors for length and time, together with Maxwell's equations (1)–(3).

As previously indicated $\mathbf{v} = [v]_0\tilde{\mathbf{v}}$ with $[v]_0 = c$. The normalization of density is less obvious. Here, we define $n = (4\pi n_0)\tilde{n}$ so that $[n]_0 = 4\pi n_0$. Including the factor of 4π in the definition simplifies the analysis elsewhere. These scaling relations apply on a species-by-species basis as well. Thus, with the current of species s defined as $\mathbf{J}_s = q_s n_s \mathbf{v}_s$, the current scales as $\mathbf{J}_s = 4\pi n_0 ec\tilde{\mathbf{J}}_s$ so that $[J]_0 = 4\pi n_0 ec$.

Here, we use the fact that $q_s = \pm e$ while $\tilde{q}_s = \pm 1$, depending on the sign of the charge on species s. Balancing the terms in Ampère's law (2) together with the fact that $\nabla = d_{i0}^{-1}\tilde{\nabla}$ and $\partial_t = \omega_{pi0}\tilde{\partial}_t$, the conversion factor for both $\mathbf{E}$ and $\mathbf{B}$ are $[E]_0 = [B]_0 = [J]_0/\omega_{pi0} = (4\pi n_0 m_i c^2)^{1/2}$. Finally, from Poisson's equation (1), it follows that the conversion factor for the electrostatic potential ϕ is $[\phi]_0 = [E]_0/d_{i0} = m_i c^2/e$. In other words, the potential energy $e\phi$ is normalized by the rest energy of a proton $m_i c^2 = 938$ MeV.

An alternative way to understand the conversion factors $[E]_0$ and $[B]_0$ is to note that energy density carried by electric and magnetic fields in Gaussian units is, respectively, $E^2/8\pi$ and $B^2/8\pi$. Thus, $[E]_0^2/8\pi = [B]_0^2/8\pi = n_0 m_i c^2/2$, which (except for the final factor of 2) is the natural unit of energy density when energy is normalized to the proton rest-mass energy. It can also be easily shown that the dimensionless value of the simulation magnetic field strength can be related to the Alfvén speed $V_A = B/(4\pi n_i m_i)^{1/2}$ by $\tilde{B} = V_A/c$ which also equals the frequency ratio Ω_{ci}/ω_{pi}, where $\Omega_{ci} = eB/(m_i c)$ is the ion cyclotron frequency. In all of the preceding discussion, the scaling factors can be converted to SI units by making the substitution $4\pi \to \epsilon_0^{-1} = c^2\mu_0$.

While the above normalizations allow the simulations to be evaluated in terms of physical units (e.g., B in Gauss), in the interpretation of our results, we use an alternative normalization scheme that allows for a simpler comparison between runs with different initial parameters. As will be argued in Sec. III A, the aspects of the evolution that we are focusing on remain quantitatively comparable when the initial $\beta_i = P_i/P_B$ is held constant, where $P_i = n_i k_B T_i$ and $P_B = B^2/8\pi$ are, respectively, the ion thermal pressure and the magnetic pressure, and k_B is the Boltzmann constant. An equivalent definition is $\beta_i = (v_{th,i}/V_A)^2$, where $v_{th,i} = (2k_B T_i/m_i)^{1/2}$ is the ion thermal velocity and $V_A = B/(4\pi n_0 m_i)^{1/2}$ is the Alfvén speed. In the simulations, β_i is determined by the ratio of $v_{th,i}$ and V_A, which are both parameters that are varied from run to run. The comparison between runs must be made at times corresponding to equal values of $\Omega_{ci0}t$ (not $\omega_{pi0}t$), where Ω_{ci0} varies across runs in proportion to the initial Alfvén velocity V_{A0}. The right side of Faraday's law (3) scales as V_{A0}^2 since both $\mathbf{B}$ and ∂_t scale as V_{A0}. Therefore, $\mathbf{E}$ must also scale as V_{A0}^2 since ∇ does not vary with run parameters. Since $T_{i0} \propto V_{A0}$ at constant β_{i0}, we choose a run-dependent normalization for $\mathbf{E}$ (Sec. III D) and quantities derived from $\mathbf{E}$ (Sec. III E) proportional to T_{i0}. Specifically, we multiply the conversion factors previously discussed by a factor $T_{i0}/m_i c^2$. Thus, for example, $[E] = (T_{i0}/m_i c^2)[E]_0$. Another conversion factor with a particularly straightforward physical interpretation is $[\phi] = (T_{i0}/m_i c^2)[\phi]_0 = T_{i0}/e$. In other words, the parameter-independent potential energy $e\phi$ (at constant β_i) is scaled by the ion thermal energy T_{i0}. Other conversion factors will be discussed at the point they are employed.

B. Field decomposition: Electromagnetic vs electrostatic

Any vector field $\mathbf{V}$ can be expressed as a sum of a divergence-free and a curl-free part, with the proviso that a spatially uniform vector field $\langle \mathbf{V} \rangle$ can be included as part of either or both components. In this study, we apply this decomposition primarily to the electric field $\mathbf{E}$ and refer to the curl-free part as *electrostatic* (ES) and the divergence-free part as *electromagnetic* (EM). These components are alternatively referred to as *irrotational* and *solenoidal* (Pongkitiwanichakul *et al.*, 2021). Thus,

$$\mathbf{E}(\mathbf{x}, t) = \mathbf{E}_{ES}(\mathbf{x}, t) + \mathbf{E}_{EM}(\mathbf{x}, t), \tag{4}$$

where

$$\mathbf{E}_{ES} = \nabla\left[\nabla^{-2}(\nabla \cdot \mathbf{E})\right]. \tag{5}$$

The symbol ∇^{-2} is the inverse Laplacian and is easily computed in Fourier space (which is well-defined for the periodic boundary conditions employed in the simulations described here) as multiplication by $-1/k^2$ for $k \neq 0$. The $k = 0$ component is the arbitrary constant field previously mentioned, which is typically set to zero. In Poisson's Eq. (1), $\nabla^{-2}(\nabla \cdot \mathbf{E}) = \nabla^{-2}(4\pi\rho) = -\phi$, so $\mathbf{E}_{ES} = -\nabla\phi$ obeys the standard definition of an electrostatic field.

We will use the same *ES* and *EM* notation for other vector fields as well, such as the current $\mathbf{J}$. Of course, $\mathbf{B}$ has no ES component since $\nabla \cdot \mathbf{B} = 0$. Thus, we can split and rearrange Ampère's law (2) into two parts

$$\mathbf{J}_{EM} = -\frac{1}{4\pi}\frac{\partial \mathbf{E}_{EM}}{\partial t} + \frac{c}{4\pi}\nabla \times \mathbf{B}, \tag{6a}$$

$$\mathbf{J}_{ES} = -\frac{1}{4\pi}\frac{\partial \mathbf{E}_{ES}}{\partial t}. \tag{6b}$$

While extracting the *scalar* potential ϕ from the total electric field is straightforward, extracting the *vector* potential from a divergence-free field, such as $\mathbf{A}$ from $\nabla \times \mathbf{A} = \mathbf{B}$, is less so. However, for 2D simulations in the x–y plane (i.e., where $\partial_z \equiv 0$), A_z can be numerically evaluated as

$$A_z(\mathbf{x}) = A_z(\mathbf{x}_0) + \int_{\mathbf{x}_0}^{\mathbf{x}} \mathbf{B}_{2D} \times d\mathbf{s}, \tag{7}$$

where $\mathbf{B}_{2D}$ is the projection of $\mathbf{B}$ into the x–y plane, and the integral is along any path between the starting point $\mathbf{x}_0$ and $\mathbf{x}$ following a path with differential element $d\mathbf{s}$. Paths that are piecewise parallel to the Cartesian directions x and y are computationally natural choices and are used to compute the magnetic field lines (contours of constant A_z) in all of the 2D plots.

The quantity $A_z(\mathbf{x}_0)$ is a constant of integration that controls the location of the contours, but not their spacing, which is proportional to $|\mathbf{B}_{2D}|^{-1}$. We choose $\mathbf{x}_0$ to be the point $(x_0, y_0) = (0, 15)d_{i0}$, which is halfway (in y) between the two initial CSs, where $\mathbf{B}$ exhibits minimal change over the course of the simulation. Thus, by setting $A_z(\mathbf{x}_0) = 0$, independent of time, the contours of A_z represent the *same* 2D field lines at different times (e.g., as in Fig. 2) to a reasonable degree of approximation.

While the decomposition of a vector field after removing any nonzero spatial average into a curl-free (*ES*) and divergence-free (*EM*) part is well-defined mathematically, the two components of the electric field, $\mathbf{E}_{ES}$ and $\mathbf{E}_{EM}$ play different physical roles in the dynamics of island coalescence. Specifically, $\mathbf{E}_{ES}$ is associated with charge separation via Poisson's equation (1), whereas $\mathbf{E}_{EM}$ is associated with time-varying magnetic fields via Faraday's law (3). The two components of $\mathbf{E}$ are then coupled via Ampère's law (2), and its decomposition into *EM* and *ES* parts (6a) and (6b). In Sec. III E 3 and the Discussion of Sec. IV, the interplay between these different components is interpreted based on the results of the numerical simulations.

C. Simulation setup

For this study, all simulations are $2\frac{1}{2}$ D (also referred to as 2D3V) and performed in a box of size $L_x \times L_y = 50d_{i0} \times 30d_{i0}$ on a grid of dimension $N_x \times N_y = 640 \times 384$, where x and y are the direction of the reversing magnetic field and the current-sheet normal, respectively. Periodicity along x is assumed. Each simulation is initialized with a pair of oppositely directed current sheets located at $y_1 = L_y/4 = 7.5d_{i0}$ and $y_2 = 3L_y/4 = 22.5d_{i0}$ such that the integrated out-of-plane current I_z vanishes, thereby allowing for periodic boundary conditions in y as well. The initial profile of the reversing magnetic field $B_x(y)$ takes the following form:

$$B_x(y) = B_{x0}\left[\tanh\left(\frac{y-y_1}{\delta_1}\right) - \tanh\left(\frac{y-y_2}{\delta_2}\right) - 1\right], \quad (8)$$

where δ_1 and δ_2 are the respective widths of the current sheets at $y = y_1$ and $y = y_2$. Thus, $B_x = -B_{x0}$ at the periodic boundaries $y = 0$ and $y = L_y$, while $B_x = +B_{x0}$ at the midline $y = L_y/2$. Equation (8) assumes that the distances from the center of each current sheet y_j to periodic boundaries at $y = 0$ and $y = L_y$ are large compared to the widths δ_j for $j = 1, 2$. In this study, we restrict consideration to the case where $\delta_1 = 0.5d_{i0}$ and $\delta_2 = 0.05d_{i0}$. We note that δ_2 is less than the grid spacing $\Delta_y = \Delta_x = 0.078d_{i0}$, so the current is largely localized to a single grid point in y. Even for the lower (thicker) sheet the distance to the nearest boundary at $y = 0$ is $15\delta_1$ for $L_y = 30d_{i0}$. Our focus will be on the *upper* current sheet at $y = y_2$, which is deliberately chosen to be much thinner than the plasmoid-chain instability threshold (Loureiro and Uzdensky, 2015).

As discussed in Sec. I, there are reasons why one would not find reconnecting CSs in the solar wind as thin as δ_2 in our simulations; either due to suppression of reconnection in the presence of asymmetry together with a guide field (Swisdak *et al.*, 2003) or disruption by plasmoid chain formation before the CS becomes that thin (Loureiro and Uzdensky, 2015). Nevertheless, the decision to use such a thin initial CS was made to ensure that the simulation domain was sufficiently small and the run times sufficiently short for computational efficiency in the context of a parameter study, while allowing for an initial set of islands to undergo many generations of merging—as discussed below in relation to Fig. 2. We hypothesize a similar multigenerational sequence of island mergers in the actual solar wind, but beginning with the tearing of a thicker current sheet and progressing over large regions in both the L and N directions, and evolving over longer time scales. These differences in both spatial and temporal scale would impose prohibitive demands on simulations that must resolve kinetic phenomena at the d_e scale.

There are a number of advantages to employing a simulation domain with two oppositely directed CS of differing width, thereby allowing for periodicity in the y direction:

(1) Periodic boundary conditions in y are less susceptible to numerical artifacts than the conducting boundary conditions need to simulate a single CS.
(2) Fully periodic boundary conditions permit the use of Fourier methods for evaluating the terms in Maxwell's equations.
(3) A spatially uniform electric field $\langle \mathbf{E} \rangle$ that cannot be identified uniquely with either $\mathbf{E}_{EM}$ or $\mathbf{E}_{ES}$ (see Sec. II B) is time independent under periodic boundary conditions. Thus, if $\langle \mathbf{E} \rangle$ initially vanishes, it will do so throughout the simulation run. The same applies for $\langle \mathbf{J} \rangle$.
(4) The thicker initial CS with $\delta_1 = 0.5d_{i0}$, while also unstable to tearing, evolves much more slowly than the thinner CS and, therefore, interferes minimally with the thinner CS over the duration of the simulation run.

Each current sheet is initialized as an approximate force-free equilibrium with $\mathbf{J} \| \mathbf{B}$. While rigorous force-free kinetic equilibria have been developed (Allanson *et al.*, 2016; Wilson *et al.*, 2018; Neukirch *et al.*, 2020), we simply impose the initial current by adding a drift velocity to a Maxwellian distribution. For our initial conditions where $\mathbf{B} = \mathbf{B}(y)$, with $B_y(y) = 0$, the orientation of $\mathbf{B}$ in the x–z plane can vary its orientation, but its magnitude is independent of y. We, therefore, must include a y-dependent guide field $B_z(y)$, where $B_z(y) = [B_{z0}^2 + B_{x0}^2 - B_x^2(y)]^{1/2}$. Here, B_{z0} is the initial guide field asymptotically far from the current sheet. Since the initial state is in pressure balance, the density at $t = 0$ is also independent of y. All of the primary runs have $B_{z0} = B_{x0}$, corresponding to a typical solar-wind shear angle of $\Delta\theta = 90°$. Guide-field dependence is addressed in Sec. IV C.

Both electrons and ions—with artificial mass ratio $m_i/m_e = 256$—are modeled as isotropic Maxwellians with run-dependent temperature $T_e = T_i$. The initial current $\mathbf{J}(y) = c\nabla \times \mathbf{B}(y)/4\pi$ is incorporated into the initial conditions by imposing a uniform drift parallel to $\mathbf{B}$ proportional to

$$\left|\frac{\nabla \times \mathbf{B}(y)}{\mathbf{B}(y)}\right| = -\frac{B_{x0}^2 - B_x^2(y)}{[B_{x0}B_z(y)]\delta} \quad (9)$$

for a current sheet of width δ. Evaluating the maximum current $\mathbf{J} = 4\pi\nabla \times \mathbf{B}/c$ at the center of each sheet yields the following expression for the electron–ion drift (assuming quasineutrality):

$$\frac{v_i - v_e}{V_{A0}} = \left(\frac{B_{x0}}{B_0}\right)\left(\frac{d_{i0}}{\delta}\right), \quad (10)$$

where $B_0 = (B_{x0}^2 + B_{z0}^2)^{1/2}$. In our initial condition, this current is carried exclusively by electrons. Under this condition, the maximum electron drift in the center of the current sheet normalized to the electron thermal velocity is

$$\frac{v_{ed0}}{v_{th,e0}} = 6.3 \times 10^{-2}\left(\frac{B_{x0}}{B_0}\right)\left(\frac{\delta}{d_{i0}}\right)^{-1}\beta_e^{1/2}. \quad (11)$$

D. Model parameters

The PIC simulations employed to study the origin and evolution of tripolar guide field perturbations observed in reconnecting solar wind current sheets (Eriksson *et al.*, 2014, 2015) require an appropriate choice of model parameters. Two key parameters set the velocity scales of the simulation. The first is the Alfvén speed as a fraction of the speed of light (V_A/c) and the second is the temperature (where we assume $T_e = T_i$ for initially isotropic electrons and protons) such that each species s has thermal velocity $v_{th,s} = (2k_BT_s/m_s)^{1/2}$. A recent statistical survey of solar-wind parameters at 1 AU (Klein and Vech, 2019, replacing their subscript p for protons with i) gives the following range for the Alfvén speed: $V_A = [23.1: \mathbf{43.5}: 70.8]$ km/s, the proton temperature $T_i = [3.2: \mathbf{10.7}: 28.1]$ eV, and the electron temperature $T_e = [8.4: \mathbf{12.7}: 18.8]$ eV, where the numbers in brackets mark the borders of the tenth percentile, the median value (bold), and the 90th

percentile. (For clarity, we suppress the Boltzmann constant k_B when expressing temperatures in units of eV.) Accommodating these small values with V_A/c in the range of 10^{-5}–10^{-4} in simulations would be prohibitively costly. We, therefore, considered whether the ratio $v_{th,i}/V_A$ provides a better characterization of the plasma environment than the thermal and Alfvén speeds taken individually. This conjecture is equivalent to having β_i play a determining role in the evolution of the current sheet since $\beta_i = (v_{th,i}/V_A)^2$. According to the table of Klein and Vech, $\beta_i = [0.37: \mathbf{1.14}: 3.04]$ (based on the parallel proton temperature).

Since the simulation box size is specified in multiples of d_{i0}, which depends on the plasma density, we note the range at 1 AU (Klein and Vech, 2019) to be $n_i = [2.52 : \mathbf{5.46} : 12.7]$ cm^{-3}, with the corresponding range for the proton inertial length being $d_i = [64.0 : \mathbf{97.6} : 144]$ km. Based on these values, we will take as a typical value $d_{i0} = 100$ km for the purpose of interpreting the simulation output in physical units. This value for d_{i0} also implies our simulation box corresponds to a physical domain of $L_x \times L_y \approx 5000 \times 3000$ km^2.

III. NUMERICAL RESULTS

A. Parameter study

Before further considering the details of tripolar guide-field generation in the presence of island coalescence, we first performed a parameter study in which we varied both the Alfvén speed and ion thermal velocity for different values of $\beta_i = (v_{th,i}/V_A)^2$. Specifically, the guide-field perturbation $(B_z(x,y) - B_{z0})/B_{z0}$ at the end of each run is plotted in Fig. 1 for eight parameter sets corresponding to five different values of β_i. Only the upper half of the simulation box ($15d_{i0} \le y \le 30d_{i0}$) associated with the initially thinner current sheet is displayed. Except for the smallest and largest values of $\beta_i = 0.0008$ and $\beta_i = 8$, respectively, two different combinations of V_{A0} and T_{i0} (or, equivalently, $v_{th,i}$) are chosen to yield each of the three intermediate values of $\beta_i = 0.08$, 0.5, and 2.0. The right column for these cases, which are aligned vertically, are for runs with higher values of both V_{A0} and T_{i0}. All runs use a time step $\Delta t = 1.72 \times 10^{-3}\Omega_{ci}^{-1}$. Thus, the time step is variable in units of ω_{pi0}^{-1}, which is the time unit in the simulation code, since $\omega_{pi0}/\Omega_{ci0} = c/V_{A0}$, and the Alfvén speed differs from run to run.

Even though each run starts from the same initial particle distributions (with velocities of species s scaled in proportion to $T_s^{1/2}$), the subsequent evolution is essentially chaotic in that the spatial distribution of islands at late times is unpredictable, with no discernible correlation between runs with different parameter values. Nevertheless, our primary diagnostic, the guide magnetic field perturbation $\delta B_z = (B_z - B_{z0})/B_{z0}$ can be compared *qualitatively* for the different runs.

Immediately obvious is the difference in character of δB_z for runs with $\beta_i < 1$ and $\beta_i > 1$. In the higher-β_i regime, δB_z is dominated by small (d_{i0}-scale) structures localized in both x and y. These small structures, however, are embedded in larger elongated islands characterized by weaker guide-field perturbations. As we are not focusing on this regime here, we will not discuss the details of these runs except to note that the two $\beta_i = 2$ runs [panels (d) and (d')] are qualitatively much closer to one another than to the $\beta_i = 8$ run [panel (e)]. The two $\beta_i = 0.5$ runs [panels (c) and (c')] are again qualitative more similar to one another than to runs with different values of β_i. However, they are closer in appearance to the runs with lower values of β_i than to those with higher values.

The low-β_i runs [panels (a), (b), and (b')] all show well-defined islands with the largest positive (red) δB_z perturbation in the center, surrounded by narrow bands of negative (blue) δB_z. As for the higher β_i values, the two runs with $\beta_i = 0.08$ [panels (b) and (b')] are qualitatively more similar to one another than to the run with β_i two orders of magnitude smaller [panel (a)]. The differences, however, are subtle, with the higher β_i resulting in islands somewhat narrower in y.

Based on this parameter study, we infer that the value of β_i plays a much greater role in determining evolution of the system than the particular values of V_{A0} and T_{i0} that jointly control the value of β_i independently do. Our analysis of the origin of the tripolar δB_z perturbations in the sections that follow will take the run corresponding to Fig. 1(b') as representative of the low-β_i regime. In doing so, an obvious question arises as to why analyzing this run is preferable to analyzing the run corresponding to Fig. 1(b), despite the latter having both V_{A0}/c and T_{i0} closer to actual solar-wind parameters. Because answering this question depends on relations explored in the course of our analysis, we defer further discussion of this point until Sec. III E 1.

Using Eq. (11), the initial force-free current in the center of the upper (narrow) current sheet for our representative low-β_i run with $B_{x0} = B_0/\sqrt{2}$ and $\beta_e = \beta_i = 0.08$ is carried by electrons with a maximum drift velocity of $v_{de0} = 3.15 v_{th,e0}$. We note that the maximum electron drift (relative to the thermal velocity) is an order of magnitude larger for the parameters of Fig. 1(a).

B. Evolution of an initially thin current sheet

A sequence of snapshots showing the evolution of δB_z in the upper half of our nominal run is presented in Fig. 2. The upper thin current sheet initially undergoes rapid tearing (panel a) resulting in a string of d_{i0}-scale islands by time step 500 ($t = 0.86\Omega_{ci}^{-1}$). Since $B_{z0} = B_{x0}$, the initial fractional perturbation δB_z at the center of the sheet ($y = 22.5d_{i0}$) is $2^{1/2} - 1 \approx 0.41$, and is uniform in x. The maximum δB_z of ~ 0.6 in Fig. 2(a) represents an $\sim 46\%$ increase over the initial maximum value. This increase is compensated by the regions of negative δB_z on the edges of the small islands, in keeping with the fact that $\partial_t \delta B_z \propto (\nabla \times \mathbf{E})_z$ averaged over a periodic domain in x and y must vanish.

By $\Omega_{ci}t = 3.43$ [panel (b)] at time step 2000, the number of identifiable islands is approximately a factor of two smaller due to early island mergers. By this time, the distinctive pattern of a narrow ribbon of negative (blue) δB_z, which persists throughout the remainder of the run, has developed. Another factor of ~2 reduction in the number of islands has occurred by time $\Omega_{ci}t = 13.72$ [panel (c)] at time step 8000. The merged islands are larger in both x and y. However, the maximum δB_z in the center of the islands has increased only slightly from the initial value of 0.41 to $\delta B_z \approx 0.8$. We note that this is approximately the maximum value for the entire run.

The rate of island coalescence slows significantly beyond this point. Nevertheless, the two relatively close times $\Omega_{ci}t = 13.72$ and 17.15 [panels (c) and (d)] at time steps 8000 and 10 000 are chosen because there are three pairs of islands undergoing coalescence during this interval. Specifically, the pair of islands between $x \sim 30d_{i0}$ and $40d_{i0}$ [panel (c)], which have already begun to merge, have mostly completed the merging process at the later time [panel (d)]. Meanwhile, two sets of islands comprising pairs at the earlier time [panel (c)]—the first pair between $x \sim 15d_{i0}$ and $x \sim 28d_{i0}$, and the second pair spanning the periodic boundary between $x \sim 41d_{i0}$ and

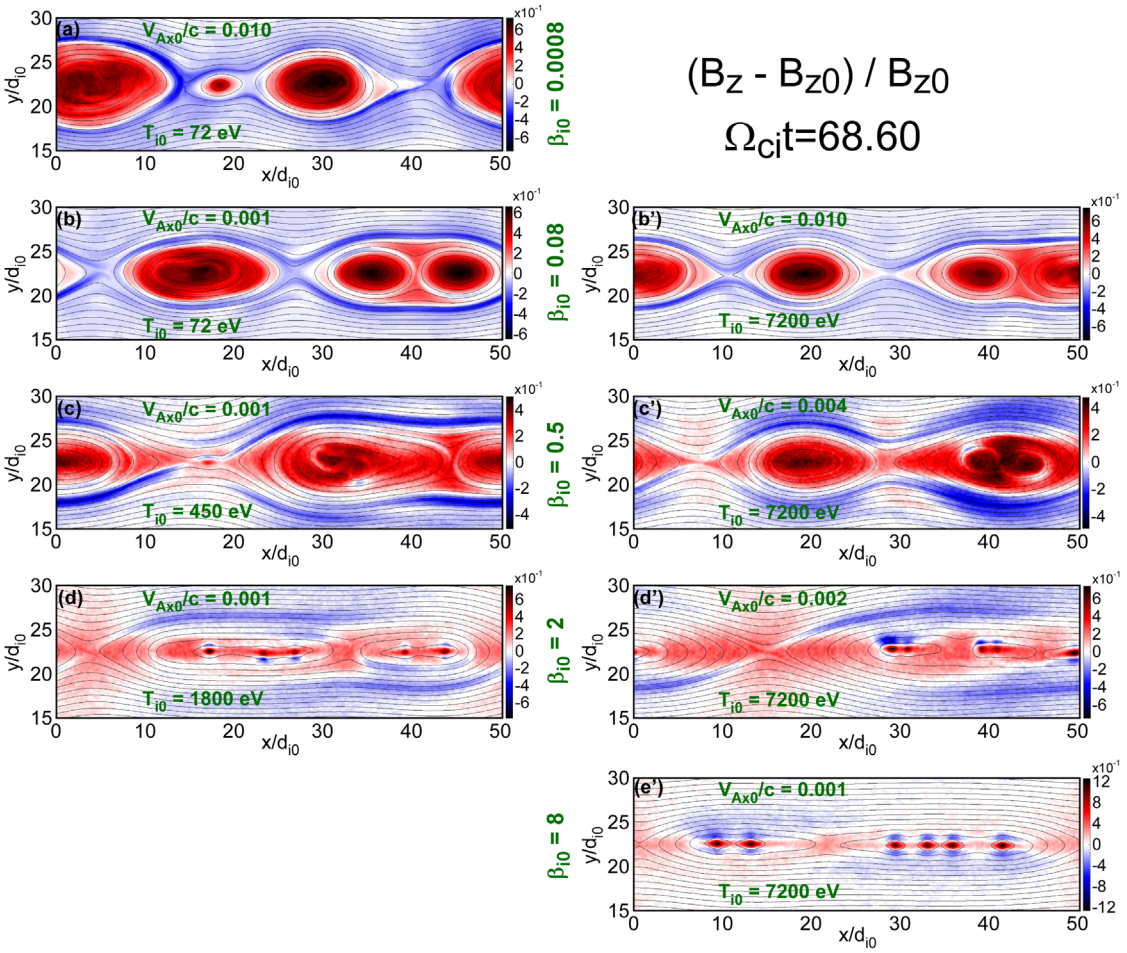

FIG. 1. Perturbed guide field $(B_z - B_{z0})/B_{z0}$ at time step 40 000 (end of run) $\Omega_{ci}t = 68.60$ for eight combinations of V_{Ax0}/c and T_{i0} corresponding to five different values of β_i: (a) $\beta_i = 0.0008$; (b) and (b') $\beta_i = 0.08$; (c) and (c') $\beta_i = 0.5$; (d) and (d') $\beta_i = 2$; and (e') $\beta_i = 8$. Note that V_{Ax0} is the Alfvén speed based on the asymptotic reversing magnetic field B_{x0} only while β_i is based on the total (reversing plus guide) magnetic field.

$x \sim 4d_{i0}$—have not yet undergone a significant degree of coalescence. However, by the later time [panel (d)], they are in approximately the same early state of merging as the pair between $x \sim 30d_{i0}$ and $40d_{i0}$ [panel (c)] previously referred to. These similarities will provide a basis for comparing key diagnostics across multiple similar coalescence events. For other diagnostics, we will focus specifically on the single time $\Omega_i t = 17.15$ [panel (d)] at time step 10 000.

Figures 2(d)–2(f) together with Fig. 1(b') are each separated sequentially by 10 000 time steps revealing occasional additional island merging events. The islands separated by the X-line in Fig. 2(d) near $x = 4d_{i0}$ slowly merge over the remainder of the simulation. The two islands separated by the X-line near $x = 42d_{i0}$ in Fig. 2(f) only begin to merge during the final 10 000 time steps of the simulation. In both of these cases, the *qualitative* behavior of the diagnostics discussed in detail below are similar to the merging events previously referenced with regard to Figs. 2(c) and 2(d). Nevertheless, we have not performed an in-depth analysis of the later island mergers.

C. Currents associated with guide-field perturbation

According to Ampère's law (2), in the absence of the displacement current $\dot{\mathbf{E}}/4\pi$, which is typically much smaller than the *physical* current $\mathbf{J}$, one can determine $\mathbf{J}$ directly from the magnetic field: $\mathbf{J} \approx c\nabla \times \mathbf{B}/4\pi$. The electron and ion components of the current are plotted in Fig. 3 at time $\Omega_{ci}t = 17.15$ (time step 10 000). The scaling factor for the plotted current, $[J]$ is defined in Sec. II A such that the magnitude of the current $\mathbf{J}$ in dimensional units equals $[J]$ for flow velocities equal to the initial ion thermal velocity $v_{th,i}$ for the nominal (initial) density n_0.

The components of the electron and ion currents are plotted in the local field-aligned-coordinate (FAC) basis in preference to the simulation Cartesian coordinates. We define our FAC basis vectors as follows: $\hat{\mathbf{e}}_{\parallel} = \hat{\mathbf{b}} = \mathbf{B}/|B|$; $\hat{\mathbf{e}}_{\perp 1} = (\hat{b} \times \hat{z})/|\hat{b} \times \hat{z}|$; and $\hat{\mathbf{e}}_{\perp 2} = \hat{\mathbf{e}}_{\parallel} \times \hat{\mathbf{e}}_{\perp 1}$, thereby forming a right-handed orthonormal set of basis vectors. According to this definition, if $\mathbf{B}$ helically wraps counterclockwise around an island (as is typical for the islands in the upper current sheet), $\hat{\mathbf{e}}_{\perp 1}$ will point outward from the center of the island and be oriented normal to the

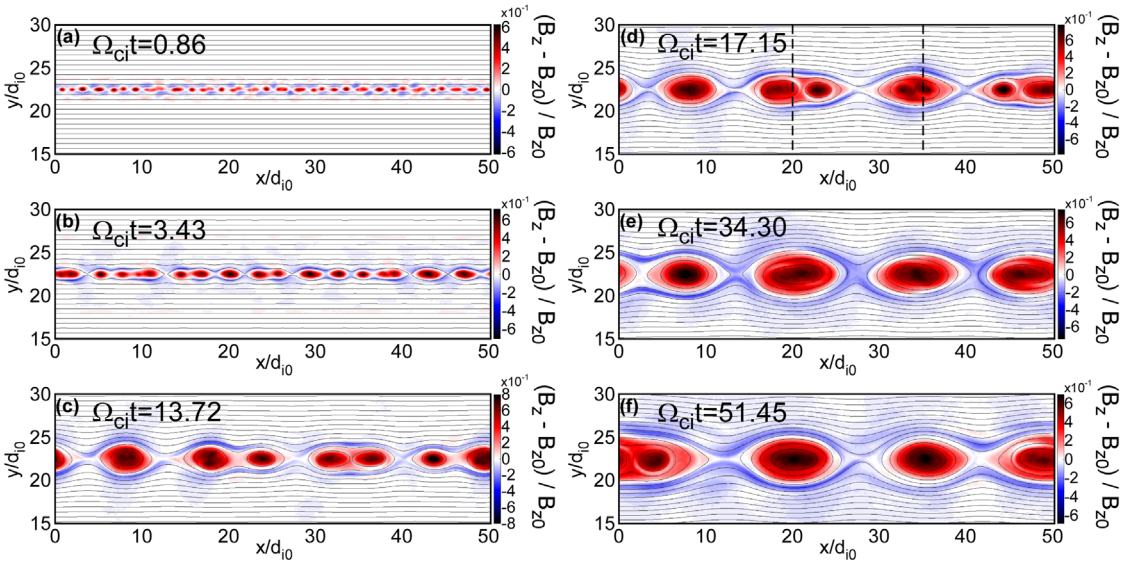

FIG. 2. Perturbed guided field $(B_z - B_{z0})/B_{z0}$ at time step (a) 500, (b) 2000, (c) 8000, (d) 10 000, (e) 20 000, and (f) 30 000 for the same run as Fig. 1(b'), which shows the same quantity at time step 40 000.

projection of **B** into the x–y plane. We will occasionally refer to the unit tangent vector of this in-plane projection of **B** as $\hat{\mathbf{e}}_{\parallel 2D}$. Because certain simulation diagnostics—especially those based on summing over particles or involving spatial derivatives—can exhibit a significant level of noise, we sometimes employ multiple iterations of nearest-neighbor smoothing (with a uniform 3×3 convolution kernel) to aid in the visualization. When employed, we note in the respective figure caption the number of iterations used.

The largest contribution to the total current is $J_{e\parallel}$ [panel (a)], which is predominantly positive (red) and almost an order of magnitude greater than $J_{i\parallel}$ [panel (a')]. The narrow regions of negative (blue) $J_{e\parallel}$ on the outer edges of merged islands is associated with the reversal of the tripolar (negative–positive–negative) guide field perturbation δB_z in Fig. 2(d). This connection was discussed in Eriksson *et al.* (2015) in terms of the projection of the parallel differential velocity into the 2D simulation plane. This projection

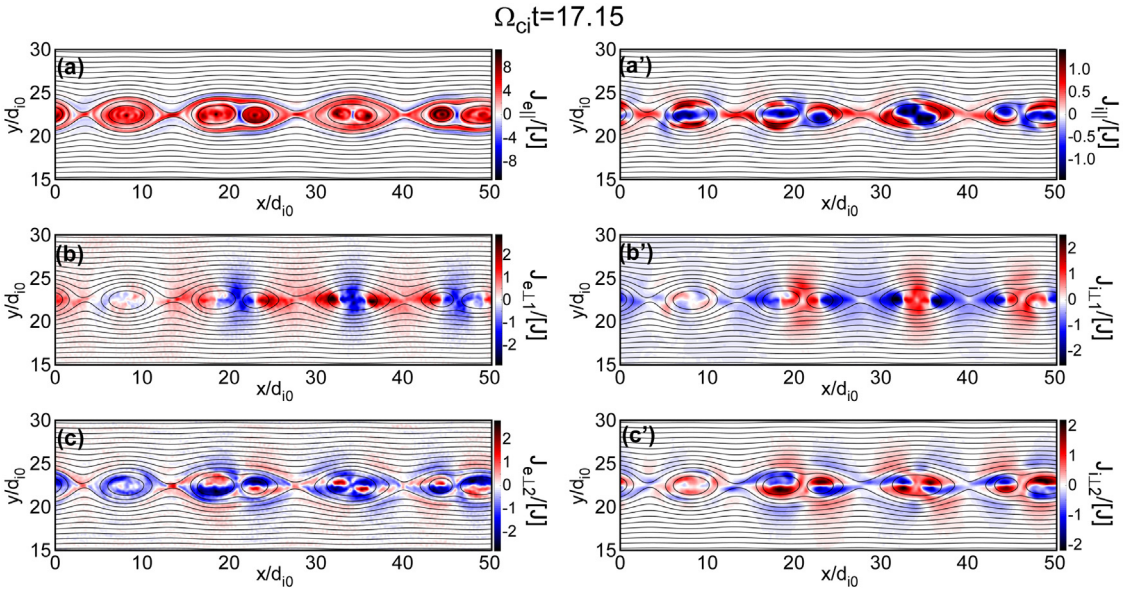

FIG. 3. Components of [(a)–(c)] electron and [(a')–(c')] ion current in field-aligned coordinates at $\Omega_{ci}t = 17.15$ (time step 10 000). [(a) and (a')] $J_{(e,i)\parallel}$; [(b) and (b')] $J_{(e,i)\perp 1}$; and [(c) and (c')] $J_{(e,i)\perp 2}$. Normalization factor $[J] = 4\pi n_0 e (T_{i0}/m_i)^{1/2}$. Four iterations of nearest-neighbor smoothing have been applied.

suppresses the strongest parallel currents near the centers of islands where **B** is almost normal to the simulation plane.

The two components of the perpendicular electron and ion currents are also typically smaller in magnitude than $J_{e\|}$ and, furthermore, are roughly equal to one another but of opposite sign. Thus, the electrons and ions have comparable perpendicular velocities indicative of both species being approximately *frozen in*. The alternating red–blue pattern in $J_{i\perp 1}$ can be understood in terms of the in-plane perpendicular flow pattern. From the definition of the basis vector $\hat{\mathbf{e}}_{\perp 1}$, $J_{i\perp 1} < 0$ (blue) corresponds to flows within the simulation x–y plane directed *inward* toward the initial current sheet or, once active X-lines have formed, as *exhaust outflow* directed toward the centers of islands. Thus, the blue regions of $J_{i\perp 1}$ correspond to the inflow above and below the active X-lines and outflow into the reconnection exhausts. The red regions, therefore, correspond to the outward bulging of the coalescing islands. The colors are reversed for $J_{e\perp 1}$ due to the opposite charge of the electron (i.e., the velocities are comparable). The direction of basis vector $\hat{\mathbf{e}}_{\perp 2}$ is harder to visualize as it points in a direction oblique to the simulation plane and is a linear combination of $\hat{\mathbf{e}}_z$ and $\hat{\mathbf{b}}_{2D}$, which is the unit vector in the direction of $\mathbf{B}_{2D}$. The approximate quadrupolar structure of $J_{s\perp 2}$ associated with pairs of merging islands is similar to the behavior of other diagnostics discussed later. We will, therefore, defer for now further discussion of this component of the current.

While $J_{e\|}$ is the largest component of the total current, it does not immediately follow that it is the dominant contributor to the tripolar δB_z via Ampère's law. To quantify the relation between δB_z and the different contributions to **J**, we use the procedure described in Sec. II B to invert the EM part of Ampère's law (6a) after first extracting the EM part of the components of **J** using Eq. (5) with **E** replaced by **J**. Figure 4 shows how the different components of **J** contribute to δB_z using the analog of Eq. (7) following the substitutions $A_z \rightarrow B_z$ and $\mathbf{B} \rightarrow \mathbf{J}$. This substitution is based on the EM part of Ampère's law (6a) with the displacement current neglected.

The perturbed guide field δB_z along the two vertical dashed lines in Fig. 2(d) are plotted as the thick black curves in panels (a) and (a') of Fig. 4 at $x/d_{i0} = 20.0$ and 35.0, respectively. The other curves are the reconstructed contributions to δB_z for the components of total current **J** as color coded by the annotations in panel (a). In both cuts, the dark blue curve due to $\mathbf{J}_{e\|}$ alone closely follows the shape of the total δB_z, especially near the outer minima that are the characteristic feature of the overall tripolar structure. However, there is a small but significant overshoot in the vicinity of the central maximum. The green curve due to $\mathbf{J}_{i\|}$ is small throughout and cannot account for the overshoot in $\mathbf{J}_{e\|}$. The thin gold and light blue curves due to $\mathbf{J}_{e\perp}$ and $\mathbf{J}_{i\perp}$ taken in isolation each have a bipolar form of significant amplitude, but are roughly equal and opposite in sign to one another, consistent with the appearance of Fig. 3 [panels (b) and (c) vs (b') and (c')]. This near cancelation is evident in the contribution from the sum $\mathbf{J}_\perp = \mathbf{J}_{e\perp} + \mathbf{J}_{i\perp}$ plotted as the red curve. This residual contribution from the total perpendicular current, nevertheless, is sufficient to almost completely account for the overshoot in the $\mathbf{J}_{e\|}$ contribution. Finally, the dashed pink curve, which is the result of reconstructing δB_z from the total current **J**, follows very closely the black δB_z curve. The small deviations can be attributed to the contribution of the displacement current $\partial \mathbf{E}/\partial t$ in Ampère's law. This deviation will be discussed later in Sec. III D.

One clear difference between the two cuts plotted, respectively, in Figs. 4(a) and 4(a') is the opposite polarities of the bipolar contributions of $\mathbf{J}_{e\perp}$ and $\mathbf{J}_{i\perp}$ to δB_z. We attribute this difference to the fact that while both cuts pass near the center of pairs of merging islands, the cut at $x/d_{i0} = 20$ transects the island on the left side while the cut at $x/d_{i0} = 35$ transects the island on the right side of the respective merging pair. Indeed, cuts through panels (c) and (c') of Fig. 3 show similar reversals in polarity in $J_{\perp 2}$ (although not in $J_{\perp 1}$).

Figures 4(b) and 4(b') plot the parallel electron current $J_{e\|}$ (black) along the same two vertical cuts at $x = 20d_{i0}$ and $x = 35d_{i0}$ along with the decomposition into ES (blue) and EM (green) parts in accordance with Eqs. (6a) and (6b). These are cuts through Fig. 3(a), but without any nearest-neighbor smoothing. The current $J_{e\|}$ in panels (b) and (b') are related to the dark blue curves in panels (a) and (a') through the integral Eq. (7) with A_z and $\mathbf{B}_{2D}$ replaced by B_z and

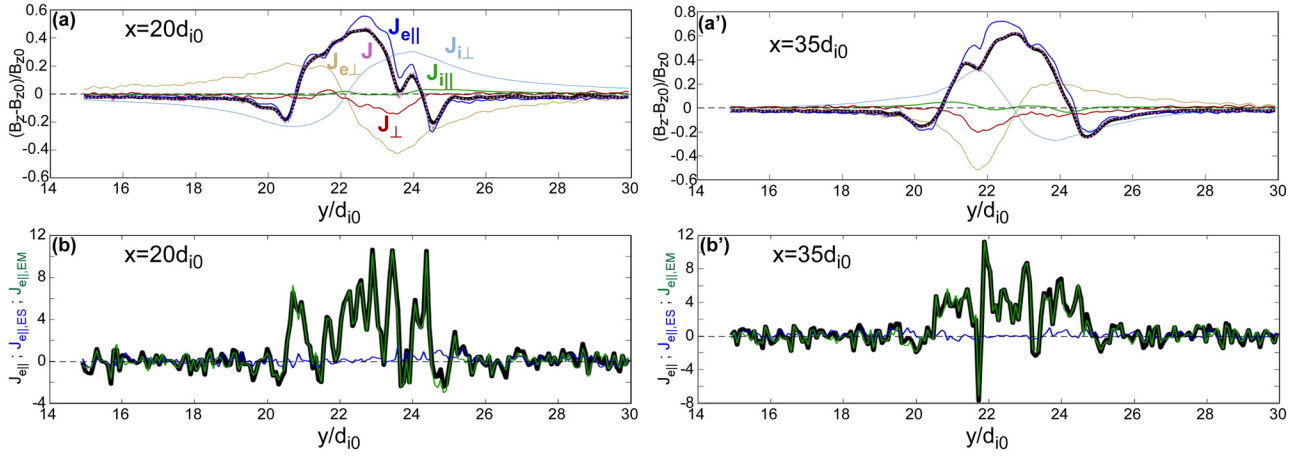

FIG. 4. [(a) and (a')] Thick black curves are cuts through guide-field perturbation δB_z at time $\Omega_{ci}t = 17.15$ [Fig. 2(d)] at (a) $x = 20d_{i0}$ and (a') $x = 35d_{i0}$. Other curves indicate contribution to δB_z from different components of the current via Ampère's law (2) as indicated in panel (a). The same color coding is used in panel (a'). [(b) and (b')] Cuts for same values of x of parallel electron current $J_{e\|}$ (black) and decomposition into curl-free (ES) and divergence-free (EM) parts (blue and green, respectively).

$\mathbf{J}_{e\parallel EM,2D}$, which is the projection of $\mathbf{J}_{e\parallel EM}$ into the x–y plane. [Recall that the right side of Eq. (7) must be divergence free.] Despite the highly structured character of $\mathbf{J}_{e\parallel}$, the resulting contribution to δB_z is quite smooth. (Note that we use vector notation $\mathbf{J}_{e\parallel}$ instead of scalar notation $J_{e\parallel}$ to emphasize that the parallel direction varies throughout the x–y plane.)

It is evident from Figs. 4(b) and 4(b') that $\mathbf{J}_{e,\parallel ES}$ is much smaller than the dominant EM component. This ordering holds for the *total* parallel current $\mathbf{J}_\parallel = \mathbf{J}_{e\parallel} + \mathbf{J}_{i\parallel}$ as well as for the total perpendicular current $\mathbf{J}_\perp$, although not for $\mathbf{J}_{e\perp}$ and $\mathbf{J}_{i\perp}$ separately, as they are essentially equal and opposite to one another. The relative insignificance of the curl-free (i.e., ES) current is a point that will be considered further in Sec. III D.

While Ampère's law without displacement current describes to a high degree of accuracy the relation between $\mathbf{J}$ and $\mathbf{B}$, the role of the electric field $\mathbf{E}$ is critical to the evolution of $\mathbf{J}$ since only electric fields can do work on the particles. Therefore, we turn now to the structure of the electric field.

D. Electromagnetic and electrostatic components of the electric field

Just as the current $\mathbf{J}$ and its components were split into curl-free (ES) and divergence-free (EM) parts in Sec. III C, we likewise contrast the ES and EM components of the electric field $\mathbf{E}$ here. Figure 5 plots the decomposition of the in-plane components E_x and E_y into ES and EM parts. Because $\partial E_z/\partial z = 0$ in a 2D simulation in the x–y plane, $E_{z,ES}$ is identically zero.

Unlike the current, for which the EM part is much larger than the ES part, the electric field exhibits the opposite ordering, although not to as extreme a degree. Here, E_x and E_y in panels (a) and (a') are qualitatively indistinguishable from $E_{x,ES}$ and $E_{y,ES}$ in panels (b) and (b'), while $E_{x,EM}$ and $E_{y,EM}$ in panels (c) and (c') are at least a factor of ∼5 smaller in magnitude and exhibit spatial characteristics distinctly different from those of the *total* E_x and E_y in panels (a) and (a'). The EM part, nevertheless, plays a critical role in the development of the tripolar δB_z guide-field perturbation because the temporal evolution of $\mathbf{B}$ is governed by Faraday's law (3), in which $\nabla \times \mathbf{E}$ effectively filters out the ES part of $\mathbf{E}$ leaving only $\mathbf{E}_{EM}$ to contribute. For example, $\partial E_{x,EM}/\partial y$ in Fig. 5(c) will contribute to $\partial B_z/\partial t$ in the regions above and below merging islands [e.g., along the cuts $x = 20d_{i0}$ and $x = 35d_{i0}$ in Fig. 2(d)].

The balance between the ES and EM part of $E_\parallel$ is different from that just discussed for E_x and E_y, as seen in Fig. 6. Instead of the ordering $|E_{x,EM}| < |E_{x,ES}| \approx |E_x|$ (and likewise for E_y, where the absolute value here indicates the range of magnitudes), $E_\parallel$ obeys the ordering $|E_\parallel| < |E_{\parallel,ES}| \approx |E_{\parallel,EM}|$. In other words, $E_{\parallel,EM} \approx -E_{\parallel,ES}$ as evident in a comparison of panels (a) and (b) of Fig. 6. For *nominal* solar wind conditions at 1 AU ($T_{i0} \sim 10$ eV and $d_{i0} \sim 100$ km), $E/[E] = 1$ corresponds to an electric field $E \sim 0.1$ mV/m, which is comparable to measured E-fields such as $\Delta E_N = 0.22$ mV/m in Eriksson *et al.* (2014).

The out-of-plane electric field E_z (not shown) is very similar in appearance and magnitude to $E_{\parallel,EM}$. However, in a 2D simulation in the x–y plane, $E_{z,ES} \equiv 0$ so that E_z is purely EM. Therefore, $E_{\parallel,EM}$ can be viewed as a proxy for E_z, which is often referred to as the *reconnection electric field* since when positive it "drives" (via $\mathbf{E} \times \mathbf{B}$ motion) the plasma and the frozen in field lines toward the X-line along y (inflow) and away from the X-line along x (exhaust outflow). This interpretation accounts for the similarity between $E_{\parallel,EM}$ in Fig. 6(b) and the in-plane perpendicular ion current $J_{i\perp 1}$ in Fig. 3(b')—except for the sign difference due to the definition of $\hat{\mathbf{e}}_{\perp 1}$.

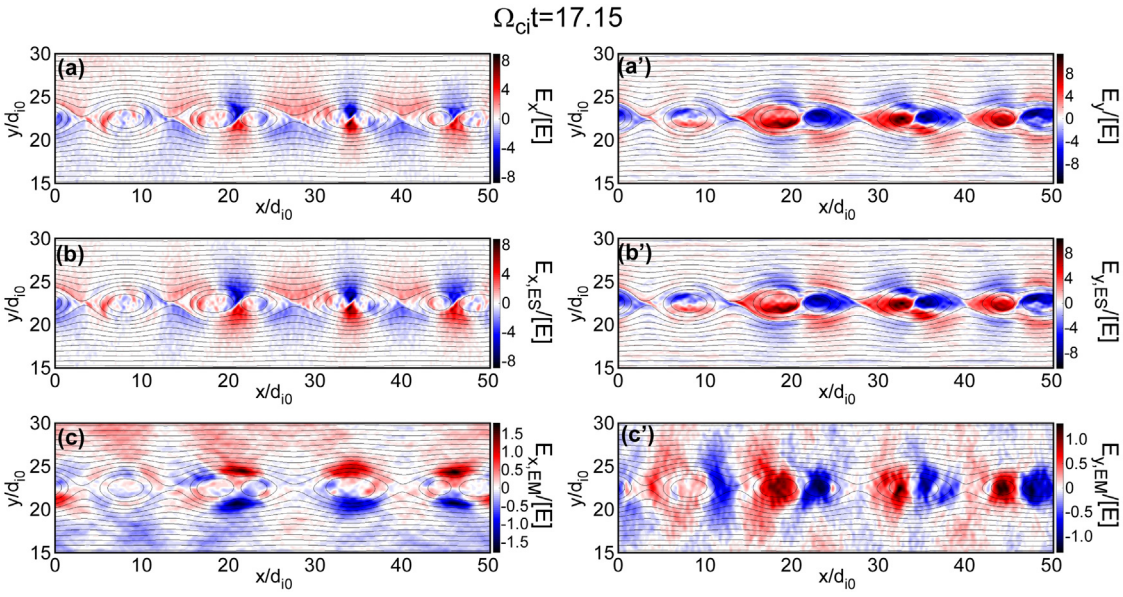

FIG. 5. In-plane components of the electric field at time $\Omega_{ci}t = 17.15$ (time step 10 000) and their decomposition into ES (curl-free) and EM (divergence-free) parts. [(a) and (a')] x and y components of total electric field; [(b) and (b')] corresponding ES parts; and [(c) and (c')] corresponding EM parts. The conversion factor from code to physical units is $[E] = [\phi]/d_{i0} = T_{i0}/(ed_{i0})$. All images were subject to four iterations of nearest-neighbor smoothing.

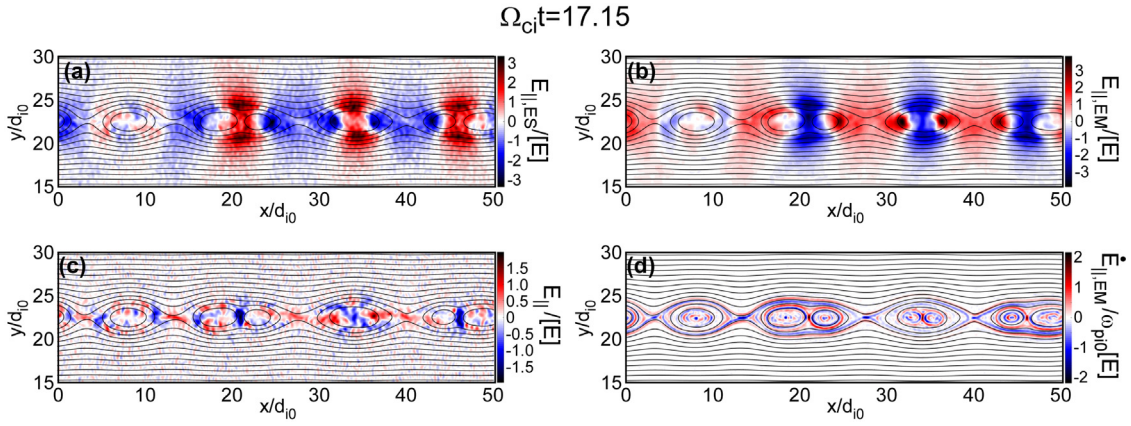

FIG. 6. Parallel electric field and its time derivative (a) ES part $E_{\parallel,ES}(x,y)$; (b) EM part $E_{\parallel,EM}(x,y)$; (c) total $E_\parallel$; and (d) time derivative of EM part from Ampère's law (2). All images subject to four iterations of nearest-neighbor smoothing.

The near cancelation of the EM and ES parts of $\mathbf{E}_\parallel$ is understandable given the fact that a highly conducting plasma cannot easily support an electric field parallel to $\mathbf{B}$ due to the high mobility of electrons along magnetic field lines. However, how this balance is maintained is not trivial—in part because the magnetic field lines are curvilinear (e.g., helical). If a substantial $\mathbf{E}_\parallel$ were to develop, electrons moving along field lines faster than the ions would result in charge separation, thereby modifying $\mathbf{E}_{ES}$. At the same time, the currents that a residual $\mathbf{E}_\parallel$ would drive can temporarily cause an imbalance between $(\nabla\times\mathbf{B})_\parallel$ and $4\pi\mathbf{J}_\parallel$, thereby modifying $\mathbf{E}_{EM}$ via the displacement current in Ampère's law. Figure 6(d) plots the divergence-free (EM) part of the instantaneous parallel displacement current $\dot{\mathbf{E}}_{\parallel,EM}=c(\nabla\times\mathbf{B})_\parallel-4\pi\mathbf{J}_\parallel$ (the ES part is negligible). The values are several orders of magnitude larger than $\dot{\mathbf{E}}_{\parallel,EM}$ found by taking finite differences in the time domain and dividing by the output interval. This discrepancy suggests that $\dot{\mathbf{E}}_{\parallel,EM}$ determined from Ampère's law is associated with high-frequency fluctuations. These fluctuations appear to be associated with the structure of $J_{e\parallel}$ in Figs. 4(b) and 4(b'). Given the alignment of $\dot{\mathbf{E}}_{\parallel,EM}$ in Fig. 6(d) with the in-plane magnetic field contours, it is reasonable to conclude that these fluctuations are not statistical in nature (i.e., a result of particle noise).

E. Quantities derived from the electric field

The curl-free and divergence-free parts of the electric field, $\mathbf{E}_{ES}$ and $\mathbf{E}_{EM}$ provide information about different aspects of island coalescence. While $\mathbf{E}_{ES}$ is associated with the charge separation ρ and electrostatic potential ϕ via Poisson's Eq. (1), $\mathbf{E}_{EM}$ is associated with the evolution of the magnetic fields via Faraday's law Eq. (3). This latter dependence appears to play an important role in the origin of the tripolar guide-field perturbations δB_z at the heart of this study. These quantities inferred from the decomposition of $\mathbf{E}$ are plotted in Fig. 7 at two different times, $\Omega_{ci}t=13.72$ (time step 8000) and $\Omega_{ci}t=17.15$ (time step 10 000), to illustrate common features associated with earlier and later phases of the merging of pairs of islands.

The different stages of island coalescence are most easily seen for the two times being considered in Figs. 2(c) and 2(d). At the earlier time ($\Omega_{ci}t=13.72$), the pair of islands on opposite sides of $x\approx 33d_{i0}$ are starting to coalesce whereas the pairs of islands on opposite sides of $x\approx 22d_{i0}$ and $x\approx 46d_{i0}$, while approaching one another, are still separated by a gap. (We will refer to this as the central pair and outer pairs.) At the later time ($\Omega_{ci}t=17.15$), the islands constituting the central pair have now largely merged, although two distinct maxima of δB_z are still evident. At this later time, the two outer pairs are at approximately the same stage of merging as the central pair was at the earlier time.

While the pairs of merging islands meet at X-lines, these can be thought of as regions of *anti-reconnection* where field lines oppositely directed in y reconnect to form lines oppositely directed in x; with the normal directions of inflow and outflow also reversed (i.e., inflow is along x and outflow along y). We contrast this situation with the *active* X-lines near $x\approx 29d_{i0}$ and $x\approx 40d_{i0}$. To provide further context for the details of island merging and the contrast with reconnection at active X-lines, the fractional electron density perturbation $(n_e-n_0)/n_0$ is plotted for the two times under consideration in Figs. 7(a) and 7(a'). Since the plasma is *quasineutral*, the corresponding ion density perturbations are virtually indistinguishable from those of the electrons. The active X-lines are characterized by significant negative (blue) density perturbations forming *channels* along the upper-left and lower-right separatrix branches. Weaker positive (red) perturbations can be observed along the opposite two separatrix branches. This asymmetry is typical of reconnection in the presence of a significant guide field (Ricci *et al.*, 2004; Eriksson *et al.*, 2015). By contrast, the merging islands are dominated by large positive perturbations associated with the centers of the previously separated islands now in the process of coalescence. Negative perturbations are also observed along the upper-right and lower-left anti-reconnection separatrix branches—especially during the early merger phases near $x\approx 33d_{i0}$ in Fig. 7(a) and near $x\approx 22d_{i0}$ and $x\approx 46d_{i0}$ in Fig. 7(a'). These features of the electron (and ion) density are reflected in features of the much smaller charge separation, as determined from $\nabla\cdot\mathbf{E}$, as discussed next.

1. Electrostatic signatures

Taking the divergence of the electric field $\nabla\cdot\mathbf{E}=\nabla\cdot\mathbf{E}_{ES}$ reveals the charge separation $n_i-n_e=\rho/e=(\nabla\cdot\mathbf{E})/4\pi e$, which is shown

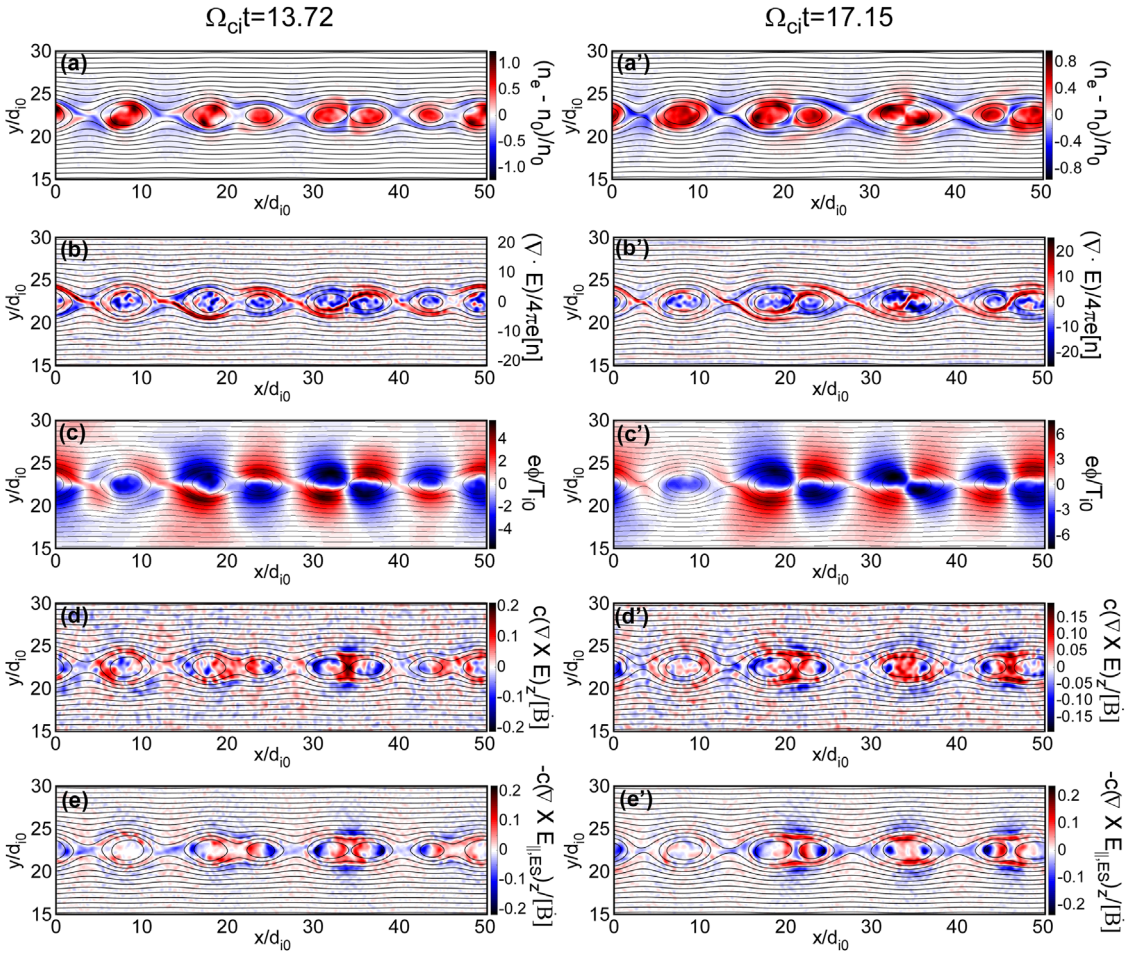

FIG. 7. Quantities related to $\mathbf{E}_{ES}$ and $\mathbf{E}_{EM}$ at two times associated with different stages of island merging. [(a) and (a')] Electron density perturbation $(n_e - n_0)/n_0$; [(b) and (b')] density imbalance $(n_i - n_e) = \nabla \cdot \mathbf{E}/4\pi e$; [(c) and (c')] electrostatic potential $\phi = -\nabla^{-2}(\nabla \cdot \mathbf{E})$; [(d) and (d')] $\dot{B}_z = c(\nabla \times \mathbf{E})_z$; and [(e) and (e')] $\dot{B}_z$ under the approximation $\mathbf{E}_{EM} = -\mathbf{E}_{ES,\|}$ so that the *EM* and *ES* parts of $\mathbf{E}_\|$ largely cancel one another (see discussion in text). The electric field scale factors are $[n] = n_0(T_{i0}/m_i c^2)$ and $[\dot{B}] = \Omega_{ci0} B_{z0}$. Four iterations of nearest-neighbor smoothing are used in panels [(a) and (a')] and [(c) and (c')], with ten iterations used in all other panels.

for the two chosen times in Figs. 7(b) and 7(b'). The scale factor $[n] = n_0(T_{i0}/m_i c^2)$ allows for an approximate scaling for different combinations of V_{A0} and T_{i0} that yield the same value for β_i as discussed in Sec. III A. In the simulation, we are focusing on the parameters of Fig. 1(b'), $T_{i0} = 7200$ eV so that $T_{i0}/m_i c^2 = 7.7 \times 10^{-6}$ corresponding to a maximum density imbalance of $(n_i - n_e)/n_0 \approx 1.5 \times 10^{-4}$. Thus, the conditions for quasineutrality are very well satisfied. For realistic solar wind temperatures of $T_i \sim 10$ eV, the density imbalance would be almost three orders of magnitude smaller. In fact, even with $T_i = 72$ eV, as for Fig. 1(b), the smallness of the density imbalance results in much less reliable electric field diagnostics. This is a primary reason for choosing the run for Fig. 1(b') rather than the one for Fig. 1(b) as the focus of this study.

Before discussing the charge imbalance in pairs of merging islands, it can be seen in Figs. 7(b) and 7(b') that the signature near the active X-lines mirrors the behavior of the electron density perturbation [panels (a) and (a')], but with the sign reversed. Thus, the channels of depressed density (both electrons and ions) is associated with a small excess of positive charge. Since these channels are aligned with the in-plane projection of **B**, the positive charge imbalance in the center of the channel can be attributed to electrons being more highly magnetized with a small gyroradius suppressing transport perpendicular but not parallel to **B**. While this inverse correlation between $n_i - n_e$ and $n_e - n_0$ is roughly valid throughout, there are clear deviations—especially within pairs of merging islands where the charge separation is more highly structured.

The structure of the charge imbalance in the vicinity of pairs of merging islands correlates with the stage of the coalescence, as can be seen by comparing Figs. 7(b) near $x \approx 33d_{i0}$ and 7(b') near $x \approx 22d_{i0}$ and $x \approx 46d_{i0}$. In all three cases, the positively charged region is characterized by a *sigmoid* shaped ribbon separating two larger negative regions. At the later time of panel (b'), the merger near $x \approx 33d_{i0}$ has progressed and the red ribbon has become more vertical while the blue regions of negative charge imbalance have become more focused

and have exhibited a degree of clockwise rotation relative to the anti-reconnection X-line. We will consider the source of this behavior later in Appendix A 2.

By inverting Poisson's Eq. (1), the electrostatic potential ϕ can be extracted from the charge density $\rho = e(n_i - n_e)$, as plotted in Figs. 7(c) and 7(c'). The pattern consisting of alternating regions of positive and negative potential can be interpreted as having approximate quadrupolar symmetry about either the active X-lines or the centers of island merging—but with opposite polarity for the two interpretations. However, in light of the irregular behavior between the active X-line near $x \approx 4d_{i0}$ and the one near $x \approx 13d_{i0}$, the latter interpretation is the more consistent one. The similarity between the shape of four lobes surrounding $x \approx 33d_{i0}$ in Fig. 7(c) and those surrounding $x \approx 22d_{i0}$ and $x \approx 46d_{i0}$ in Fig. 7(c') further support this interpretation. Thus, one can infer a direct connection between these quadrupolar potential signatures of island merging and the corresponding regions of charge imbalance in Figs. 7(b) and 7(b'). We note that this quadrupolar potential pattern is distinct from the trapping electrostatic potentials in the inflow region of single X-line reconnection (e.g., Egedal *et al.*, 2008; Egedal, Daughton, and Le, 2012; Haggerty *et al.*, 2015). These trapping potentials, identified as $\Phi_\parallel$, are computed by integrating $\mathbf{E}_\parallel$ along magnetic field lines. As noted by Egedal *et al.* (2008), $\Phi_\parallel$ can differ significantly from the standard potential ϕ found by inverting Eq. (1). Since the method for integrating $\mathbf{E}_\parallel$ along field lines is not well suited for cases where the field lines encircle magnetic islands, evaluation of $\Phi_\parallel$ has not been undertaken in this study.

The inferred scaling of ϕ with T_{i0} at constant β_i would imply a maximum potential of $\phi \sim \pm 50$ V for realistic solar wind parameters. There are qualitative and quantitative correlations between the gradients of ϕ in Fig. 7(c') and the components $E_{x,ES}$ and $E_{y,ES}$ in Figs. 5(b) and 5(b'). For example, the local minimum and maximum of $e\phi/T_{i0} \sim \pm 5$ at $(x, y) \sim (24, 21)d_{i0}$ and $(24, 24)d_{i0}$, respectively, are consistent with an $E_{y,ES} = -\partial_y \phi \sim 1.25[E]$ in Fig. 5(b') averaged over the vertical line segment connecting the minimum and maximum of ϕ.

2. Electromagnetic signatures

We now turn to the divergence-free part of the electric field: $E_{x,EM}$ and $E_{y,EM}$ plotted in Figs. 5(c) and 5(c'). Although smaller in amplitude than the corresponding curl-free (ES) components, the EM part of $\mathbf{E}$ plays a critical role in the development of the tripolar guide-field perturbation δB_z because only $\mathbf{E}_{EM}$ contributes to $\dot{\mathbf{B}} \propto \nabla \times \mathbf{E}$ via Faraday's law (3). If we focus on the pair of merging islands near $x \approx 33d_{i0}$ at $\Omega_{ci}t = 13.72$ in Fig. 7(d), a region of maximal $\dot{B}_z > 0$ (red) near the anti-reconnection X-line is surrounded by four (blue) minima where $\dot{B}_z < 0$ above and below as well as to the left and right of the central maximum. We argue that it is the vertically displaced minima that account for the negative excursion of δB_z above and below the merging islands.

Comparing $\dot{B}_z$ for the same merging pair at $\Omega_{ci}t = 17.15$ in Fig. 7(d') reveals an outward (vertical) displacement of both the negative region and positive region closer to midplane at $y \approx 22.5d_{i0}$. This outward motion is consistent with the evolution of δB_z between the same two times in Figs. 2(c) and 2(d). Specifically, as the (negative followed by positive) pulse in $\dot{B}_z$ moves outward, δB_z first decreases and then increases as the ribbon of negative δB_z also propagates outward. We note that at the later time of Fig. 7(d'), the pattern of regions where $\dot{B}_z < 0$ near the merging island pairs at $x \approx 22d_{i0}$ and $x \approx 46d_{i0}$ resemble the pattern at $x \approx 33d_{i0}$ at the earlier time in panel (d).

The regions of negative $\dot{B}_z$ displaced in x to the left and right of the anti-reconnection X-line have a different interpretation: By comparing the relative location of the maxima of δB_z associated with the two merging islands near $x \approx 33d_{i0}$ in Figs. 2(c) and 2(d), one sees that as they move closer together, they leave behind a region of less-positive δB_z where the island centers were at the earlier time; hence, $\dot{B}_z < 0$ at those locations.

While we have focused on specific island coalescence events between $\Omega_{ci}t = 13.72$ and $\Omega_{ci}t = 17.15$ in Fig. 7, these events follow upon previous generations of island coalescence, as seen in Fig. 2. Evidence of a negative δB_z perturbation outside the separatrix layers appears as early as panel (b) at $\Omega_{ci}t = 3.43$. Thus, the proposed mechanism for driving these perturbations based on panels (d), (e), (d'), and (e') of Fig. 7 can be thought of as a *pump* that adds to the cumulative negative δB_z signature that includes contributions from earlier coalescence events. However, the subsequent evolution of regions of negative δB_z as it expands along field lines outside the separatrix layers cannot be followed via its time derivative in light of the noise level evident in Figs. 7(d) and 7(d').

3. Relation between electrostatic and electromagnetic fields

The analysis presented in Sec. III E 2 identified the source, via Faraday's law (3), of the reversal in δB_z resulting in the characteristic tripolar character associated with merging islands. However, the description was merely descriptive and did not provide an explanation as to *why* $E_{x,EM}$ and $E_{y,EM}$ have the structure seen in Figs. 5(c) and 5(c'), which results in $\dot{B}_z$ having the structure seen in Figs. 7(d) and 7(d'). We now present evidence for the origin of the observed behavior of $\mathbf{E}_{EM}$, although a discussion of the underlying mechanism is deferred until Sec. IV B.

It was shown in Fig. 5 that in the simulation (x–y) plane, the amplitude of $\mathbf{E}_{ES}$ is significantly larger than that of $\mathbf{E}_{EM}$. However, along the direction parallel to the local magnetic field, $E_{\parallel,ES}$ and $E_{\parallel,EM}$ are approximately equal but opposite to one another, as seen in Fig. 6. We note that this difference between the in-plane and parallel decomposition of $\mathbf{E}$ into $\mathbf{E}_{ES} + \mathbf{E}_{EM}$ is not simply due to the orientation of $\mathbf{B}$ relative to the x–y plane, but is also related to the fact that in a 2D simulation $E_{z,ES} = 0$, which implies $E_{z,EM} = E_z$.

As previously mentioned, the approximate vanishing of $\mathbf{E}_\parallel$ is a consequence of the ease with which electrons can move parallel to $\mathbf{B}$. Here, we make the *Ansatz* that any parallel electron flow induced by a residual $\mathbf{E}_\parallel$ will induce a change to $\mathbf{E}_{EM}$ so as to counter that residual parallel field. Consequently, we hypothesize that $\mathbf{E}_{\parallel,EM} \approx -\mathbf{E}_{\parallel,ES}$, where $\mathbf{E}_{\parallel,ES}$ is due to the in-plane charge separation plotted in Figs. 7(b) and 7(b'). To test this hypothesis, we computed $\dot{B}_z$ from Faraday's law (3) under the approximation $\mathbf{E} \equiv -\mathbf{E}_{\parallel,ES}$. The result is plotted in Figs. 7(e) and 7(e') for the two times being considered. The agreement with the actual $\dot{B}_z$ in panels (d) and (d') is quite good except in the vicinity of the midplane $y \approx 22.5d_{i0}$. This disagreement, which also fails to account for the out-of-plane electric field driving reconnection near active X-lines, is presumably due to the fact that computing $\nabla \times \mathbf{E}_{\parallel,ES}$ requires projection from the direction $\hat{\mathbf{b}}$ back into the x–y plane, which is ill conditioned near the midplane where $\hat{\mathbf{b}}$

is nearly orthogonal to the x–y plane. These differences, however, are not relevant to the formation of the tripolar δB_z characteristic of island merging. According to our *Ansatz*, the origin of the tripolar δB_z can, therefore, be traced back to the charge separation proportional to $\nabla \cdot \mathbf{E}$ in Figs. 7(b) and 7(b'), which is responsible for $\mathbf{E}_{ES}$ in Figs. 5(b) and 5(b'). It should be emphasized that $-\mathbf{E}_{\parallel,ES}$ is not divergence free, but does contain a significant divergence-free (i.e., EM) part. It is this EM part that produces the approximation to $\dot{B}_z$ in Figs. 7(e) and 7(e'). These issues are discussed further in Sec. IV.

IV. DISCUSSION

The preceding analysis of the simulations undertaken provide empirical evidence for an electrostatic field due to charge separation playing a key role in the generation of a tripolar guide-field perturbation δB_z characteristic of reconnection in a thin current sheet following the merging of island pairs. Specifically, it is argued that if an electromagnetic field develops that approximately cancels the projection of $\mathbf{E}_{ES}$ along $\mathbf{B}$, then the curl of that field generates a temporal variation $\dot{B}_z$ in the out-of-plane magnetic field in the direction opposite to the prevailing guide field. This interpretation requires that the following two questions be addressed: (1) How do the dynamics of islands merging result in the pattern of charge separation observed in the simulations? and (2) How does the resulting ES field lead to an approximate equal and opposite EM response? We consider these two questions in turn next, followed by a brief examination of how the process of island coalescence varies as a function of the initial guide-field ratio.

A. Dynamics of island coalescence

If we use the guide-field perturbation δB_z as an indicator of how islands merge, the progression in Fig. 2 suggests that regions of high δB_z develop in the interior of islands as they approach one-another and transition fairly smoothly from multiple maxima to a single maximum inside a new larger island. For example, the two pairs of maxima near the vertical dashed lines in Fig. 2(d) have each merged into a unimodal δB_z maximum by the time of Fig. 2(e). Other diagnostics, such as the charge separation in Figs. 7(b) and 7(b') are more structured, with both positive and negative perturbations in the vicinity of the merging islands.

We emphasize the charge separation here because of the important role played by $\mathbf{E}_{ES}$ as summarized below in Sec. IV B. However, the structure of the electron density in Figs. 7(a) and 7(a') is qualitatively similar to the structure of the charge separation $\propto \nabla \cdot \mathbf{E}$ in Figs. 7(b) and 7(b'), but of opposite sign. Since the plasma is quasineutral with $n_i - n_e \ll n_i \sim n_e$, plots of the ion density are virtually indistinguishable from plots of the electron density. Nevertheless, the small difference between them is essential for the existence of $\mathbf{E}_{ES}$. The maxima of n_e are particularly large, for example, in the region $30d_{i0} \leq x \leq 40d_{i0}$ in Fig. 7(a'). These maxima are suggestive of compression or focusing of the electrons (and, therefore, the ions as well) in the cores of the two islands undergoing coalescence. The fact that these density maxima are associated with minima in the charge density [panel (b')] indicates that the electrons are slightly more focused than the ions. This relation is consistent with the electrons being more strongly tied to the field lines, which point primarily in the $\hat{z}$ direction near the maxima, than the ions with their larger gyroradius.

We present in Appendix A an illustrative example of how the evolution of the magnetic field and the electron flow differ by following, respectively, the evolution of magnetic field lines, which remain parallel to the instantaneous value of $\mathbf{B}$ and the evolution of electron flow lines, which, under several simplifying assumptions, are parallel to the instantaneous electron fluid velocity. Specifically, it is assumed that the electron velocity *perpendicular* to $\mathbf{B}$ is dominated by the $\mathbf{E} \times \mathbf{B}$ drift velocity, which has been confirmed via direct comparison for the spatial region and time range under consideration. A second, more approximate assumption is that a single average value for the electron flow velocity *parallel* to $\mathbf{B}$ is used without accounting for spatial and temporal variations. Despite these approximations, the resulting field and flow lines correspond well with the actual evolution of δB_z and the charge separation (proportional to $\nabla \cdot \mathbf{E}$), as depicted in Figs. 9 and 10, respectively. Nevertheless, we present the results in Appendix A as a plausible explanation for the difference observed in the simulations pending a more rigorous derivation,

In Sec. IV B, we connect these and previous findings to construct a model by which the concentration of electron charge in localized spatial regions associated with merging islands contributes to the development of the tripolar δB_z signature observed in the simulations—and characteristic of *in situ* observations in the solar wind.

B. Physical interpretation of tripolar δB_z generation mechanism

Interpreting the origin of the tripolar δB_z perturbation based on the 2D simulations presented here relies heavily on the splitting of vector fields into curl-free (ES) and divergence-free (EM) parts. While $\mathbf{B}$ is, by definition, always divergence free, both $\mathbf{E}$ and $\mathbf{J}$ (the other vectors participating in Maxwell's equations) can, in general, contain both ES and EM parts. The relations between these parts are expressed in Eqs. (6a) and (6b). Furthermore, Eq. (5) describes how $\mathbf{E}_{ES}$ is derived from $\nabla \cdot \mathbf{E}$, which, as discussed in Appendix A 2 appears to be related to behavior of electron flow lines.

Despite the fact that $\mathbf{J}_{ES}$ is associated with $\partial \mathbf{E}_{ES}/\partial t$ via (6b) and $\mathbf{J}_{EM}$ is associated with $\partial \mathbf{E}_{EM}/\partial t$ via (6a), the balance between the EM and ES parts of $\mathbf{J}$ and $\mathbf{E}$ is quite different. As seen in Fig. 5, the in-plane x and y components of $\mathbf{E}$ are predominantly ES, with $\mathbf{E}_{EM}$ making a relatively small contribution. Of course, in a 2D simulation the out-of-plane E_z is entirely EM in nature, but still has a smaller maximum amplitude than the in-plane $\mathbf{E}_{ES}$. By contrast, $\mathbf{J}$ consists almost entirely of $\mathbf{J}_{EM}$, as seen in Figs. 4(b) and 4(b') for the decomposition of $J_{e,\parallel}$.

Because Eq. (6a) also depends on $\nabla \times \mathbf{B}$, a more appropriate comparison would be to compare the EM and ES parts of $\partial \mathbf{E}/\partial t$. The EM part, which is plotted in Fig. 6(d), is highly structured—a point we will return to shortly. However, the ES part (not plotted) is indistinguishable from the contribution of discrete particle noise. Thus, unlike $\mathbf{E}$ itself, its time derivative is predominantly EM rather than ES. We note that the smallness of $\partial \mathbf{E}_{ES}/\partial t$ determined from $\mathbf{J}_{ES}$ is consistent with estimating its magnitude through evaluating finite differences of $\mathbf{E}_{ES}$ in the time domain.

While $\mathbf{E}_{ES}$ is the dominant component of $\mathbf{E}$ in the x–y plane, the *parallel* component of $\mathbf{E}$ is small due to near cancelation of the $E_{\parallel,ES}$ and $E_{\parallel,EM}$ [see Figs. 6(a)–6(c)]. As discussed in Sec. III D, this near cancelation is a consequence of the fact that a residual *total* $E_\parallel$ can effectively drive parallel electron currents that in turn modify $\mathbf{E}$ via

Ampère's law. One can, nevertheless, ask whether $\mathbf{E}_{ES}$ is adjusting to cancel $\mathbf{E}_{EM}$ or vice versa; or, perhaps both parts are simultaneously adjusting to cancel one another. The dominance of $J_{\parallel,EM}$ over $J_{\parallel,ES}$ in Figs. 4(b) and 4(b') suggests that the interpretation whereby $\mathbf{E}_{EM}$ adjust to cancel $\mathbf{E}_{ES}$ is more consistent with the simulations.

The above interpretation is further bolstered by the favorable comparison of Figs. 7(e) and 7(e') with Figs. 7(d) and 7(d') using the *Ansatz* $\mathbf{E}_{EM} = -E_{\parallel,ES}\hat{\mathbf{b}}$. This comparison implies that when computing $\partial\mathbf{B}/\partial t$ from Faraday's law (3), replacing $\mathbf{E}_{EM}$ in its entirety with $-E_{\parallel,ES}\hat{\mathbf{b}}$ is a good approximation—especially away from the centers of the islands where the negative parts of the tripolar δB_z signature are observed. This comparison also highlights the fact that it is *only* the subdominant EM part of $\mathbf{E}$ that contributes to the temporal evolution of $\mathbf{B}$ through Faraday's law because $\nabla \times \mathbf{E}$ selects only the EM part of $\mathbf{E}$ while filtering out the (generally larger) ES part.

Piecing together the multiple diagnostics considered in this study, a source mechanism for the generation of the commonly observed tripolar δB_z signature along the exterior of merging islands can be built. The primary process is involved with the dynamical evolution of the island mergers. Specifically, the focusing of regions of negative charge density, as suggested by the flow-line tracing in Appendix A 2, serves as a source for the global ES field structure. The twisting of the flow-line centers associated with pairs of merging islands results in the chain of roughly quadrupolar electrostatic potentials of Figs. 7(c) and 7(c'). The magnitude of these potential maxima and minima are several times the ion thermal energy density, although separated by many ion inertial lengths. If the projection of $\mathbf{E}_{ES}$ in the $\hat{\mathbf{b}}$ direction were not largely canceled by an oppositely directed parallel projection of $\mathbf{E}_{EM}$, the parallel current driven by that residual $\mathbf{E}_{\parallel}$ field would in turn produce the requisite oppositely directed $\mathbf{E}_{\parallel,EM}$ via the EM part of Ampère's law (6a). Finally, the resulting $\mathbf{E}_{EM}$ drives a negative outward propagating perturbation to B_z via Faraday's law (3), which may be suppressed for higher values of β_i.

The preceding overview of the tripolar δB_z generation mechanism leaves out many important details. Most notably, the way in which parallel currents evolve so as to generate $\mathbf{E}_{\parallel,EM}$ approximately equal and opposite to $\mathbf{E}_{\parallel,ES}$ in Figs. 6(a) and 6(b) needs to be better understood. As previously mentioned, there is significant spatial structure in both $J_{\parallel,EM}$ [Figs. 4(b) and 4(b')], and in $\partial\mathbf{E}_{\parallel,EM}/\partial t$ [Fig. 6(d)]. This spatial structure is suggestive of a wave-like process being involved. We leave the resolution of this issue as a topic for future investigation.

C. Guide-field dependence

The model for the origin of tripolar guide field perturbations developed in this study have been based on simulations initialized with an initial asymptotic guide-field ratio $B_{z0}/B_{x0} = 1.0$, which corresponds to a shear angle $\Delta\theta = 90°$ across the current sheet. While these values are *typical* for CSs in the solar wind at 1 AU, observations of reconnecting current sheets (Gosling, 2012; Eriksson *et al.*, 2022) support a range of shear angles $\Delta\theta$ spanning most of the range between $\Delta\theta \lesssim 180°$ for near *antiparallel* reconnection with $B_{z0} \ll B_{x0}$, and $\Delta\theta \gtrsim 0°$ for guide-field dominant reconnection with $B_{z0} \gg B_{x0}$. Figure 8 compares the guide-field perturbation δB_z and the charge separation $\nabla \cdot \mathbf{E}/4\pi$ for guide-field ratios of $B_{z0}/B_{x0} = 0.1$, 0.5, 1.0, and 2.0, corresponding to shear angles of $\Delta\theta = 2\cot^{-1}(B_{z0}/B_{x0}) = 168.6°$, 126.9°, 90.0°, and 53.1°.

The simulation runs are all initialized with the same value of B_{x0} so that the magnitude of $\mathbf{B}_0$ scales as $(B_{x0}^2 + B_{z0}^2)^{1/2} = B_{x0}/\sin(\Delta\theta/2)$. The guide-field perturbation δB_z in the left column will be considered first. When comparing runs with different values of B_{z0}, there is no unambiguous way to choose comparable times. In Figs. 8(a)–8(d), comparable times $\Omega_{ci}t \approx 20$ are shown, where Ω_{ci} is based on the run-dependent value of $|\mathbf{B}_0|$. These times are labeled in green in the figure. For the largest guide field $B_{z0} = 2.0B_{x0}$, the coalescence process has not advanced as far at this time. Therefore, in Fig. 8(e), we consider a later time when $\Omega_{cix}t$ using the ion cyclotron frequency based on B_{x0} alone (labeled in red) is the same as for the $B_{z0} = B_{x0}$ case in Fig. 8(c). For the stronger guide-field runs, $\Omega_{cix}t$ appears to be a better indicator for comparable stages of evolution. The similarity of the locations of the islands in the runs with different B_{z0} is not coincidental since the particle distributions in all of the runs are seeded with the same set of random numbers. Only the initial electron drift velocity from Eq. (11) differs from run to run.

The intensity scale for each panel of Figs. 8(a)–8(e) is normalized to the value of B_{z0} the particular run. Therefore, the plotted value of δB_z is the *relative* rather than the *absolute* guide field perturbation. The range of the (symmetric) intensity scale is determined by the maximum positive δB_z in the centers of the islands. The regions of negative (blue) perturbation in panel (a) with $B_{z0} = 0.1B_{x0}$ are very small, both as relative and absolute quantities. Thus, there is at most a very weak tripolar signature for this large shear angle ($\Delta\theta \approx 170°$) run. Increasing B_{z0} to $0.5B_{x0}$ in panel (b) results in a significant increase in the relative $\delta B_z < 0$ guide-field perturbation, and therefore, an even larger increase in the corresponding absolute perturbation. This trend continues for $B_{z0} = B_{x0}$ (c) and $B_{z0} = 2B_{x0}$ (d) and (e).

In addition to the increase in amplitude of the negative δB_z perturbations with B_{z0}, there is also a shift in the location of the minima. For example, in Fig. 8(b) for $B_{z0} = 0.5B_{x0}$, the darkest blue regions surrounding the merged islands is offset to the left of center above and to the right of center below each large island. The corresponding offsets in Fig. 8(a) for $B_{z0} = 0.1B_{x0}$ are even more pronounced, but less obvious because of the lower amplitude of the maximum negative δB_z perturbations. For the runs with larger initial guide fields of $B_{z0}/B_{x0} = 1.0$ in panel (c) and 2.0 in panels (d) and (e), the maximum negative δB_z perturbations are mostly centered above and below the merged islands.

The offsets just described for weaker initial guide-field ratios is consistent with the interpretation put forward by Eriksson *et al.* (2014), which included the results of a PIC simulation with the same value $B_{z0}/B_{x0} = 0.5$ as in Fig. 8(b). In that study it was argued that the negative δB_z perturbations were related to the Hall magnetic field perturbation originating at the *active* X-lines between the large post-coalescence islands. These Hall-field signatures are evident in the negative (blue) regions extending along the upper-right and lower-left separatrix arms relative to the active X-lines such as the one near $x = 28d_{i0}$ in Fig. 8(b). A similar pattern is evident in panel (a) for $B_{z0}/B_{x0} = 0.1$. In fact, weak δB_z *enhancement* (red) can be seen along the lower-right separatrix branch extending from the active X-line near $x = 12d_{i0}$. This positive δB_z enhancement is a vestige of the quadrupolar Hall field associated with strictly anti-parallel reconnection with $B_{z0} = 0$ and $\Delta\theta = 180°$, where the positive and negative δB_z perturbations are of equal magnitude along opposite pairs of separatrix arms—positive along the upper-left and lower-right arms and negative along the lower-left and upper-right arms.

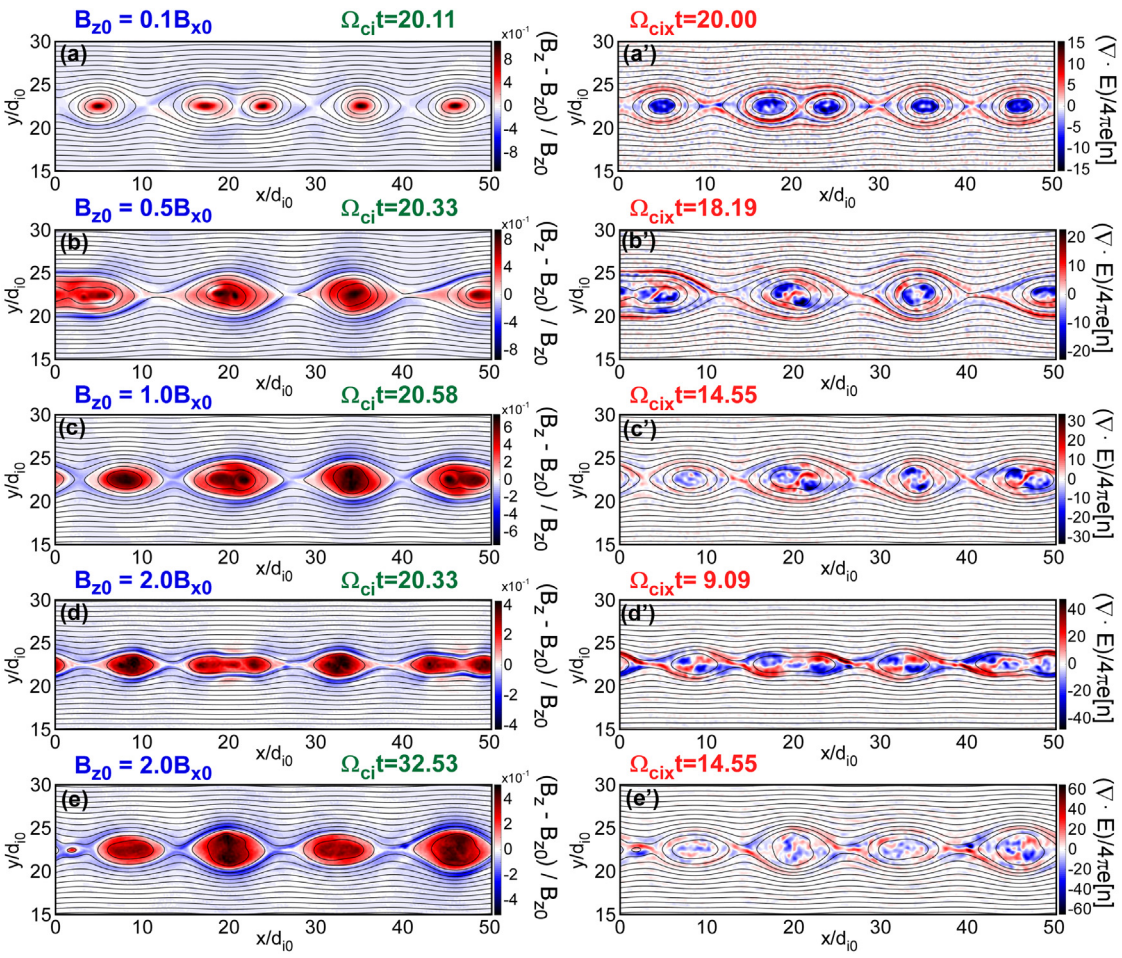

FIG. 8. Guide field perturbation δB_z [(a)–(e)] and charge separation $\nabla \cdot \mathbf{E}/4\pi$ [(a')–(e')] for different background guide fields B_{z0} with initial reversing magnetic field B_{x0} kept constant. [(a) and (a')] $B_{z0}/B_{x0} = 0.1$; [(b) and (b')] $B_{z0}/B_{x0} = 0.5$; [(c) and (c')] $B_{z0}/B_{x0} = 1.0$; and [(d) and (d')] and [(e) and (e')] $B_{z0}/B_{x0} = 2.0$. The first four rows are at the same approximate time $\sim 20\Omega_{ci}^{-1}$ for the ion cyclotron frequency based on the *total* initial asymptotic magnetic field. The final row [(e) and (e')] is at a later time when $\Omega_{cix}t$, based on the ion cyclotron frequency using the initial asymptotic *reversing* magnetic field only is the same as for panels [(c) and (c')].

The fact that the offsets in the location of the negative δB_z perturbations in Fig. 8(b) are intermediate to those in panels (a) and (c) suggest that the origin of these negative perturbations may involve a combination of influences: the Hall magnetic field from active X-lines together with the negative perturbation due to the island coalescence process discussed in Sec. IV B. An examination of the diagnostics for $\dot{B}_z$ analogous to those in Figs. 7(d), 7(d'), 7(e), and 7(e') but for $B_{z0} = 0.5B_{x0}$ reveals some evidence of a contribution from the coalescence mechanism. However, given the overall weaker δB_z magnitude for this run, the noise level in the $\dot{B}_z$ diagnostics is too large to draw a definitive conclusion. In the opposite case of the $B_{z0} = 2.0B_{x0}$ of Fig. 8(e), evidence for the role of the proposed coalescence mechanism for negative δB_z perturbations is unambiguous. We, therefore, limit our claims regarding this mechanism to the regime $B_{z0} \geq B_{x0}$, even though we suspect that it plays a role for weaker guide-field ratios as well. Therefore, although not considered explicitly in the present comparison, the mechanism associated with island coalescence should be applicable to the case with an even stronger guide-field ratio $B_{z0}/B_{x0} = 3.9$ analyzed in Eriksson *et al.* (2015).

To help better understand the role of the asymptotic guide-field ratio B_{z0}/B_{x0} or, equivalently, the shear angle $\Delta\theta$ on the development of negative δB_z perturbations, the charge separation $(n_i - n_e) = \nabla \cdot \mathbf{E}/4\pi e$ is plotted in Figs. 8(a')–8(e') for the same runs and at the same times as Figs. 8(a)–8(e). This diagnostic was chosen in light of the role ascribed in Sec. IV B to the post-coalescence charge separation as a driver of the negative δB_z perturbations. As illustrated in Appendixes A 1 and A 2 for the nominal case with $B_{z0} = B_{x0}$, the structure of positive and negative regions of charge-separation are maintained following island coalescence longer than the time required for the magnetic field structure of two initially disjoint islands to merge. Thus, over the 5.2 Ω_{ci}^{-1} spanned in panels (b')–(d') of Figs. 9 and 10, the magnetic field lines have undergone almost complete mixing while the regions of strongest negative charge density remain separated from one another.

In Fig. 8(a'), for the weakest initial guide field $B_{z0} = 0.1B_{x0}$, the charge separation shows little structure, with a largely symmetric region of excess negative charge (blue) in the center of the merged islands. The negatively charged regions largely mirror the maxima in δB_z in Fig. 8(a). Therefore, one should not expect island coalescence to play a significant role in the generation of negative δB_z perturbations for this weak guide field.

For guide field ratios of $B_{z0}/B_{x0} = 0.5$ and above [Figs. 8(b')–8(e')], there is greater structure in the charge separation $(n_i - n_e)$ than in the corresponding δB_z in the interior of post-coalescence islands, with a magnitude increasing with guide-field strength. The longevity of the charge-separation structure also increases with the strength of the initial guide-field.

V. CONCLUSIONS

The development of a characteristic tripolar pattern in the perturbation of an initial out-of-plane guide field is a robust feature of 2D PIC simulations initialized with a thin force-free CS over a range of initial guide fields—or, equivalently, magnetic rotation angles $\Delta\theta$—and for values of the ion plasma beta $\beta_i \lesssim 1$. This tripolar pattern takes the form of a negative guide-field perturbation outside the magnetic separatrices (e.g., blue regions in Fig. 2) together with guide-field enhancements (red regions) in the interior of magnetic islands. Thus, a CS in the solar wind sweeping past a satellite would exhibit temporal negative–positive–negative B_M signature for a significant fraction of satellite positions and CS velocities.

This tripolar pattern does not develop when magnetic reconnection is limited to a single X-line, in which case the B_M perturbation (B_z in the simulations) takes the form of a quadrupolar Hall field; symmetric for anti-parallel and asymmetric for guide-field reconnection. While the tripolar guide-field perturbation could be described as a modified Hall field, we generally avoid that terminology since the origin of these two phenomena are not necessarily the same.

The initialization of the simulations with a very thin CS results in the rapid formation of a plasmoid chain consisting of many very small islands. The sequential pairwise coalescence of these small islands to form fewer but larger islands appear to play a critical role in the formation of the negative B_M perturbation layers. The focus of this study has been to develop a theoretical understanding of how these negative perturbations develop. This theoretical analysis was aided by expressing the electric field in the simulation as a superposition of electromagnetic (divergence-free) and electrostatic (curl-free) parts: $\mathbf{E} = \mathbf{E}_{EM} + \mathbf{E}_{ES}$. The two components of $\mathbf{E}$ play different essential roles in the evolution. $\mathbf{E}_{ES}$ is a manifestation of charge separation, which persists in the interior of a post-coalescence merged island well after the magnetic fields wrapping the two initially separated pre-coalescence islands have become well mixed. However, only $\mathbf{E}_{EM}$ can couple to the evolving $\mathbf{B}$ through Faraday's law, thereby providing a source for the negative B_M perturbation. It is the fact that the plasma cannot easily maintain a significant $\mathbf{E}_{\|}$ that forces $\mathbf{E}_{ES\|}$ and $\mathbf{E}_{EM\|}$ to adjust to one another. Analysis of the simulation output indicates that $\mathbf{E}_{EM}$ adjusts to cancel $\mathbf{E}_{ES\|}$, which in turn generates a negative $\dot{B}_M$ outside the separatrix above and below pairs of merging islands. It is this interplay between the electrostatic and electromagnetic parts of $\mathbf{E}$ that provides the heretofore *missing link* in causal chain linking island coalescence to the development of a tripolar B_M structure.

Due to the limited box size of the simulation, the islands cannot grow beyond a width of $\sim 10d_{i0}$. This width is small compared to the widths of reconnecting CSs observed at 1 AU (e.g., Eriksson *et al.*, 2022). This scale discrepancy is consistent with the fact that the observed CSs have had a much longer time to evolve without the artificial constraint of a finite simulation box. It can be inferred that the CSs observed at 1 AU originated closer to the sun where β_i is generally smaller. Our focus has been on a simulation with a low $\beta_i = 0.08$. Such low values, while atypical at 1 AU, have been observed; but it may also be indicative of a source region nearer the sun. Based on the comparison of Fig. 1, similar evolution can be expected for β_i as large as 0.5, which is more typical at 1 AU, but not for values of $\beta_i = 2$ and larger.

Another limitation of the simulations used in this study is their restriction to two spatial dimensions. This restriction, nevertheless, rendered the interpretation of key diagnostics more tractable. The fact that tripolar B_M perturbations are observed in the solar wind, which is intrinsically 3D, suggests that the restriction of the simulations to 2D is not a fundamental limitation. Existing 3D simulations (e.g., Daughton *et al.*, 2011; Markidis *et al.*, 2013) show that interacting magnetic islands in 2D simulations assume the form of more complicated interacting flux ropes. Extending the analysis presented here into a full 3D domain is the subject of ongoing investigation.

ACKNOWLEDGMENTS

This research was supported by NASA HSR Grant No. 80NSSC19K0828. The numerical simulations were performed using resources provided by the NASA Advanced Supercomputing Division (NAS).

AUTHOR DECLARATIONS

Conflict of Interest

The authors have no conflicts to disclose.

Author Contributions

David L. Newman: Conceptualization (equal); Formal analysis (lead); Funding acquisition (supporting); Investigation (equal); Methodology (lead); Resources (equal); Software (supporting); Visualization (lead); Writing – original draft (lead); Writing – review & editing (equal). **Stefan Eriksson:** Conceptualization (equal); Formal analysis (supporting); Funding acquisition (lead); Investigation (equal); Methodology (supporting); Project administration (lead); Resources (equal); Visualization (supporting); Writing – original draft (supporting); Writing – review & editing (equal). **Giovanni Lapenta:** Conceptualization (equal); Formal analysis (supporting); Funding acquisition (supporting); Investigation (equal); Methodology (supporting); Resources (equal); Software (lead); Visualization (supporting); Writing – original draft (supporting); Writing – review & editing (equal).

DATA AVAILABILITY

The simulation data and analysis codes that support the findings of this study are available from the corresponding author upon reasonable request.

APPENDIX A: ANALYSIS OF ISLAND COALESCENCE USING VECTOR-FIELD TRACING

In this appendix, we will focus on the pair of islands that are in the process of merging between $x \approx 30d_{i0}$ and $x \approx 40d_{i0}$ starting at time $\Omega_{ci}t = 13.72$ (left column of Fig. 7) through $\Omega_{ci}t = 17.15$ (right column of Fig. 7 as well as Figs. 3 through 6), and continuing for an equal time interval ending at $\Omega_{ci}t = 20.58$ (not shown in previous figures). Specifically, we will use field-line and flow-line tracing to help understand the differences between the behavior of δB_z and the charge separation $n_i - n_e = \rho/e = \nabla \cdot \mathbf{E}/4\pi$.

Field-line tracing involves integrating parameterized curves through space that remain parallel to the local $\mathbf{B}$ along their trajectory. In 3D simulations, these curves can be quite complicated. However, in 2D simulations, the projection of the field lines into the x–y plane are the contours of constant A_z plotted in the previous figures showing different quantities as functions of x and y. Therefore, field-line tracing normally provides little information beyond what can be discerned from plots of B_z superposed on contours of constant A_z. In order to gain further insight into the dynamics of merging islands, we make the following two modifications to the field-line tracing method: First, we let the coordinate in z serve as a proxy for time through a linear relation $t = t_0 + z/\dot{z}$ for an assumed fixed value of $\dot{z}$. Second, we generalize the procedure for following *field* lines to instead trace a proxy for *flow* lines by including a term proportional to an inferred perpendicular $(\mathbf{E} \times \mathbf{B})$ *drift* motion added to the parallel motion.

The field/flow-line tracing is implemented using MATLAB (2021), by following streamlines of a specified vector field. For our purposes, these streamlines satisfy the following parametric equation:

$$\frac{d\mathbf{r}}{ds} = \hat{\mathbf{b}} + \alpha \frac{\mathbf{v}_D}{c}, \tag{A1}$$

where $\mathbf{r}$ is the position in x–y–z space, s is the integration parameter, where the unit parallel vector $\hat{\mathbf{b}} = \mathbf{B}/|B|$ and the drift velocity $\mathbf{v}_D/c = (\mathbf{E} \times \mathbf{B}/B^2)$ are both evaluated (from the simulation output) at time $t \equiv t(z)$ based on the z component of $\mathbf{r}(s)$. There are two parameters that need to be specified: $\dot{z}$ from the definition of $t(z)$; and α, which scales the contribution of the drift velocity when evaluating flow lines. In order for Eq. (A1) to produce lines parallel to the electron flow, the parameter α must be chosen so that $\alpha = c/u_\parallel$, where $u_\parallel$ is an estimate of the parallel electron flow velocity. The right side of (A1) is then proportional to $u_\parallel \hat{\mathbf{b}} + \mathbf{v}_D$. This model makes the simplifying assumption that a single value of $u_\parallel$ adequately approximates the parallel electron velocity throughout the spatial and temporal range under consideration. Assigning a specific value to α is deferred until Appendix A 2.

Regarding the parameter $\dot{z}$, there is no rigorous way to assign a unique correspondence between z and t. A seemingly more natural approach might have been to associate t with the parametric variable s. However, doing so would have resulted in a confusing graphical representation in which each slice through the field/flow lines at fixed values of z would contain information spanning a range of values of t. Alternatively, one might attempt to associate $\dot{z}$ with a natural velocity of the system (e.g., the Alfvén speed or a typical parallel electron flow velocity). This latter choice might seem particularly apt when considering electron flow lines in Appendix A 2. Instead, we choose a mapping between z and t in such a way that the field/flow lines exhibit a substantial excursion through 3D space over a period during which both $\mathbf{B}$ and $\mathbf{E}$ change by only a small amount. The relation between t and z we settle upon was determined largely through trial and error, as discussed further in Appendix A 1. Since the illustrative examples in Figs. 9 and 10 are intended to convey *qualitative* rather than *quantitative* behavior, the exact relation between t and z is not critical. However, we have confirmed that the qualitative behavior is consistent over a wide range of values for the parameter $\dot{z}$.

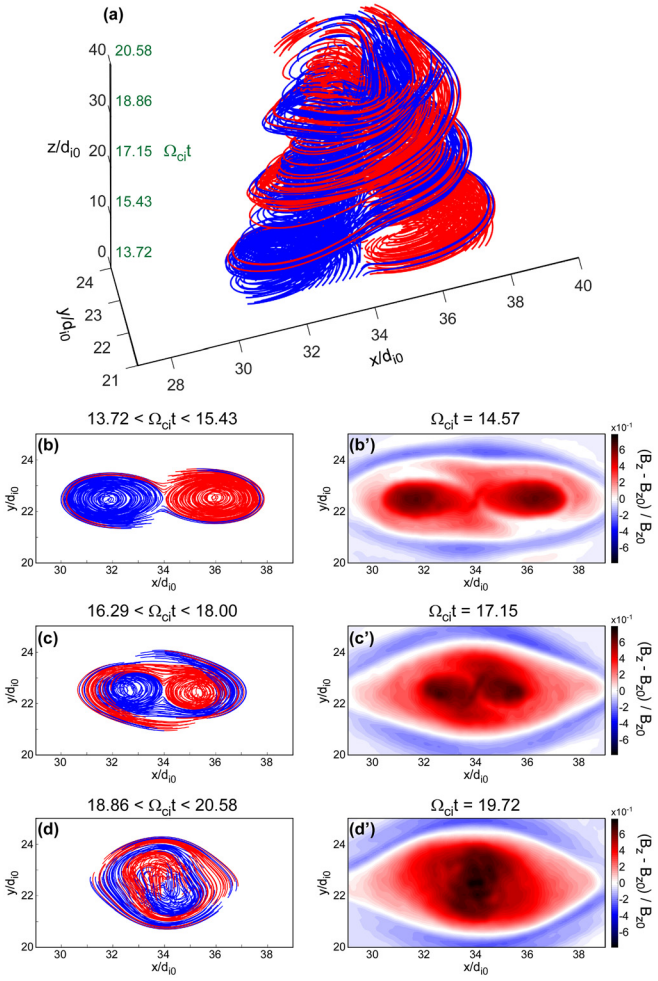

FIG. 9. Field-line tracing along curves parallel to $\hat{\mathbf{b}}(x, y, t)$ with $\Omega_{ci}t = 13.72 + 0.1715z/d_{i0}$ starting from $n_x \times n_y = 36 \times 6$ array of equally spaced points in the x–y plane (at $z = 0$) in the range $30.5 \le x/d_{i0} \le 37.5$ and $22.0 \le y/d_{i0} \le 23.0$. Field lines starting at $x < 33.9d_{i0}$ are colored blue and those starting at $x > 33.9d_{i0}$ are colored red. (a) Side view of all field lines in the range $z < 40d_{i0}$; [(b)–(d)] Top view limited to the range of z values corresponding to the time interval indicated, which correspond to $0 \le z/d_{i0} \le 10$, $15 \le z/d_{i0} \le 25$, and $30 \le z/d_{i0} \le 40$, respectively. [(b')–(d')] Plots of δB_z over the same region of th x–y plane at the midpoint of the time range spanned by the corresponding field-line plot.

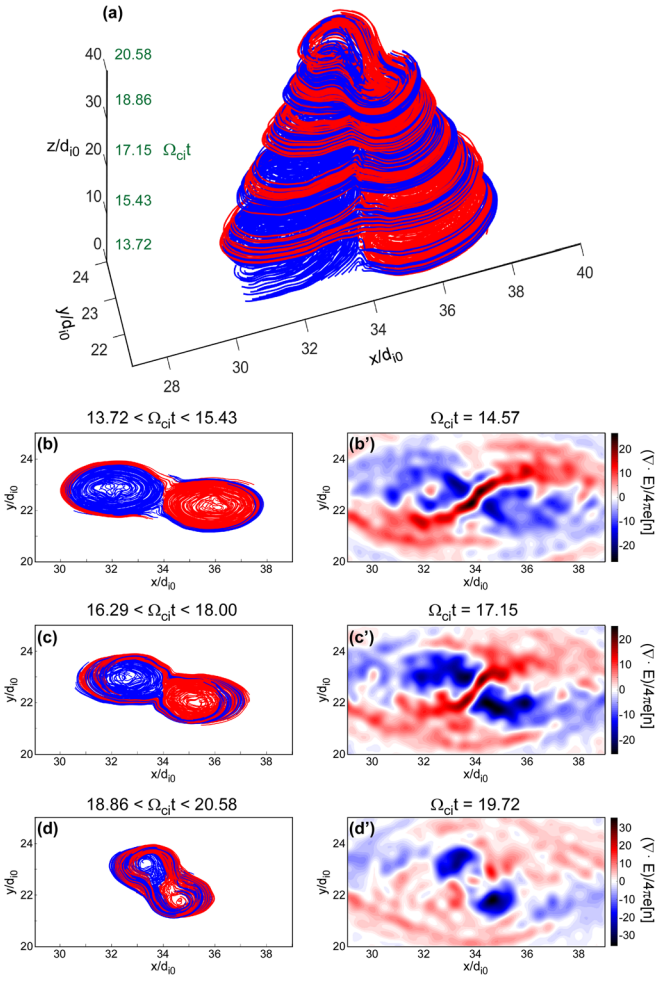

FIG. 10. [(a)–(d)] Similar to corresponding panels of Fig. 9 except line tracing follows trajectories of electrons consisting of motion parallel to **B** as well as $\mathbf{E}\times\mathbf{B}$ drift, as described in the text. [(b')–(d')] Plots of charge separation $n_i - n_e = \nabla\cdot\mathbf{E}/4\pi e$ with same normalization as in Figs. 7(b) and 7(b').

1. Magnetic field-line evolution

To study the evolution of field lines during the merging of two islands, we setup a grid of points in x and y at the initial time $\Omega_{ci}t = 13.72$ (corresponding to left column of Fig. 7) in the range $30.5 \le x/d_{i0} \le 37.5$ and $22.0 \le y/d_{i0} \le 23.0$. We identify this initial time with $z = 0$. To differentiate the field lines originating in the two initially separate islands, we color those starting with $x < 33.9d_{i0}$ as blue and those starting with $x > 33.9d_{i0}$ as red. The field lines for the entire period under consideration are plotted in Fig. 9(a), with cuts at specific times side by side with simultaneous plots of δB_z in the remaining frames.

The field lines, which satisfy Eq. (A1) with $\alpha = 0$ naturally extend in z as they circulate either about the two islands—either separately or jointly—during different states of merging. The more slowly t increases as a function of z the more times the field lines are able to wraparound the islands before reaching the end of the interval under consideration ($\Omega_{ci}t = 20.58$). In these illustrative examples, we chose a maximum excursion Δz of $40d_{i0}$ for the duration $\Delta t = 6.86\Omega_{ci0}^{-1}$, which corresponds to $\dot{z} = 5.83d_{i0}\Omega_{ci0} = 5.83V_{A0}$.

An overall sense of a transition from two separate islands near $z = 0$ to a single merged island near $z = 40d_{i0}$ can be appreciated from the oblique side view in Fig. 9(a); with red and blue field lines originally associated with the two initial islands wrapping around each other. We emphasize that the field-line color is determined solely by its original location in the x–y plane at $z = 0$. Thus, the juxtaposition of red and blue lines is an indication of mixing, with the exception of a few lines that initially wraparound the exterior of oppositely colored islands due to imperfect assignment at $z = 0$.

A clearer picture develops when looking at three localized *slices* (in both z and t) projected onto the x–y plane in Figs. 9(b)–9(d). The first (earliest) slice (b) covers the range $0 < z/d_{i0} < 10$ before significant merging of the two islands has occurred. This is evident from the well-defined segregation of the red and blue field lines. It is worth noting that if **B** were held at its starting value throughout the field-line tracing, slices over *any* comparable interval in z would look qualitatively the same. This reiterates the previous statement that field lines for a fixed time in a 2D simulation, when projected into the x–y plane, trace out contours of constant A_z.

The second slice (c), covering the range $15 < z/d_{i0} < 25$, shows the centers of the two initial islands about which the field lines are circulating to have moved closer together, with a subset of field lines having crossed the separatrix dividing the two islands and are now wrapping around the partially merged pair. The final slice (d), covering the range $30 < z/d_{i0} < 40$ shows little evidence of any remaining centers of circulation for the two initial islands, with the merger largely complete.

Despite the approximate nature of this method, the results closely mirror the behavior of the actual magnetic-field structure and seen in the corresponding plots of δB_z in the respective panels (b')–(d') covering the same region in the x–y plane. The darkest red regions in panels (b') and (c') are associated with the centers of the pre-merging and merging islands, respectively. Their locations agree well with the centers about which the field lines are orbiting in corresponding panels (b) and (c).

At the final time (d') there is now essentially one extended region where δB_z is maximal corresponding to near completion of the merging process. Although one cannot draw an exact association between the figures in panel (d') with those in panel (d), the overall size and shape of the merged islands in the two representations are quite similar. This is to be contrasted with the behavior of the *flow* lines—and the distribution of charge separations to which they are compared—as will be discussed next in Appendix A 2.

2. Electron flow-line evolution

We display electron flow lines in a manner analogous to the way the field lines were exhibited in Fig. 9, except for the fact that α assumes a nonzero value. We will be focusing in this section on the origin of the charge-separation patterns seen in Figs. 7(b) and 7(b'), which are largest in the interior of the pairs of coalescing islands. Therefore, when interpreting flow lines, we will use the parallel electron current plotted in Fig. 3(a) from these same regions for guidance. This quantity exhibits significant spatial variability—especially near an anti-reconnection X-line where the sign of the parallel

current $\mathbf{J}_{e\|}$ can reverse. However, $\mathbf{J}_{e\|}$ is predominantly positive in the interior of the merging islands under consideration. For specificity, we assume a *typical* value of $J_{e,\|}/[J] \sim 4$. Using the definition of $[J]$ from the caption of Fig. 3 (as explained in Sec. II A), with $T_{i0} = 7200\,\text{eV}$ [from Fig. 1(b')] and a physical proton mass with $m_i c^2 = 9.38 \times 10^6$ eV, a normalized parallel electron current of ∼4 corresponds to a parallel electron velocity $v_{e,\|}/c \sim 0.011$ (which we round to 0.01). We note that for a positive $J_{e,\|}$, the parallel electron flow velocity is negative. However, the results that follow depend only on the *magnitude* of $v_{e,\|}$, so we have dropped the minus sign. Given that the $\mathbf{E} \times \mathbf{B}$ drift velocity should be normalized to the characteristic parallel flow velocity (also normalized to c), we use the value $\alpha = 100$ in Eq. (A1).

Figures 10(a)–10(d) shows the evolution of electron flow lines using the same layout as Figs. 9(a)–9(d) for the field lines. However, the field-line structure was compared to the guide-field perturbation δB_z [in panels (b')–(d')], whereas the flow-line structure is compared to the charge density $\propto \nabla \cdot \mathbf{E}$. In order to simplify the comparison, we use the same value for $\dot{z}$ in both figures. While it may appear inconsistent to choose a value for $\dot{z}$ that is *not* based on the estimated parallel flow velocity, it must be reiterated that $\dot{z}$ does not correspond to a physical velocity. Instead, the flow lines should be interpreted as having characteristics at each value of z based on the $\mathbf{B}$ and $\mathbf{E}$ fields at the local time $t(z)$. In this regard, the (green) temporal values for the vertical axis in Fig. 10(a) should take precedence over the (black) spatial values. To reiterate, there is nothing *special* about the exact relation between z and t employed in these figures. It should be noted, however, that the spatial scale *does* provide a basis for visualizing the pitch of the field and flow lines in the 3D representations.

The three temporal slices projected onto the x–y plane in Figs. 10(b)–10(d) are for the same time intervals (and, therefore, ranges in z) as the corresponding panels in Fig. 9. The earliest slices are similar to one another, with field/flow lines confined largely to the island from which they originate. However, the centers about which flow lines circle exhibit a clear offset in y (positive for the left island and negative for the right island), which is a consequence of including the $\mathbf{E} \times \mathbf{B}$ drift velocity (i.e., $\alpha \neq 0$). We note that if both $\mathbf{E}$ and $\mathbf{B}$ are held constant at their starting values (i.e., for $\Omega_{ci} t = 13.72$), the flow-line structure would remain approximately the same for all three slices in z, with the same offset as in Fig. 10(b). However, unlike for the field lines, where the z-independence of the slices (for time-independent $\mathbf{B}$ and $\mathbf{E}$) is a consequence of the vanishing of $\nabla \cdot \mathbf{B}$, the z-independence is only approximate when $\alpha \neq 0$.

The flow lines in Figs. 10(c) and 10(d) show the centers of the two islands maintain their identity while wrapping around one another in a clockwise sense. This is in contrast with the field lines in Fig. 9 [especially panel (d)], where the two islands have essentially merged into one. This difference is attributable to the inclusion of the $\mathbf{E} \times \mathbf{B}$ drift in Eq. (A1) through the parameter α.

Figures 10(b')–10(d') contain plots of the normalized charge density $\propto \nabla \cdot \mathbf{E}$ for the same three slices in t and z as panels (b)–(d). [See Figs. 7(b) and 7(b') for plots showing the structure of this diagnostic over a larger spatial region.] There is a clear correspondence between the flow lines associated with the two merging islands and the (blue) minima of $\nabla \cdot \mathbf{E}$ for all three slices. This correspondence suggests a physical connection between the structure of the flow lines and the simultaneous charge density distribution. Since the minima of $\nabla \cdot \mathbf{E}$ are regions of excess electron density (relative to the ions), a plausible connection with the flow-line structure is that electrons, which exhibit motion *parallel* to $\mathbf{B}$ simultaneous with $\mathbf{E} \times \mathbf{B}$ drift motion *perpendicular* to $\mathbf{B}$, are "focused" into the regions where the flow lines circulate around their respective island centers.

REFERENCES

Akhavan-Tafti, M., Palmroth, M., Slavin, J. A., Battarbee, M., Ganse, U., Grandin, M., Le, G., Gershman, D. J., Eastwood, J. P., and Stawarz, J. E., "Comparative analysis of the vlasiator simulations and MMS observations of multiple x-line reconnection and flux transfer events," J. Geophys. Res.: Space Phys. **125**, e2019JA027410, https://doi.org/10.1029/2019JA027410 (2020).

Allanson, O., Neukirch, T., Troscheit, S., and Wilson, F., "From one-dimensional fields to Vlasov equilibria: Theory and application of hermite polynomials," J. Plasma Phys. **82**, 905820306 (2016).

Artemyev, A. V., Angelopoulos, V., Vasko, I. Y., Runov, A., Avanov, L. A., Giles, B. L., Russell, C. T., and Strangeway, R. J., "On the kinetic nature of solar wind discontinuities," Geophys. Res. Lett. **46**, 1185–1194, https://doi.org/10.1029/2018GL079906 (2019).

Borovsky, J. E., "Flux tube texture of the solar wind: Strands of the magnetic carpet at 1 AU?," J. Geophys. Res.: Space Phys. **113**, A08110, https://doi.org/10.1029/2007JA012684 (2008).

Borovsky, J. E. and Denton, M. H., "No evidence for heating of the solar wind at strong current sheets," Astrophys. J. **739**, L61 (2011).

Brackbill, J. and Forslund, D., "An implicit method for electromagnetic plasma simulation in two dimensions," J. Comput. Phys. **46**, 271–308 (1982).

Chasapis, A., Retinò, A., Sahraoui, F., Vaivads, A., Khotyaintsev, Y. V., Sundkvist, D., Greco, A., Sorriso-Valvo, L., and Canu, P., "Thin current sheets and associated electron heating in turbulent space plasma," Astrophys. J. **804**, L1 (2015).

Crooker, N. U., Burton, M. E., Phillips, J. L., Smith, E. J., and Balogh, A., "Heliospheric plasma sheets as small-scale transients," J. Geophys. Res.: Space Phys. **101**, 2467–2474, https://doi.org/10.1029/95JA03148 (1996).

Daughton, W., Roytershteyn, V., Karimabadi, H., Yin, L., Albright, B. J., Bergen, B., and Bowers, K. J., "Role of electron physics in the development of turbulent magnetic reconnection in collisionless plasmas," Nat. Phys. **7**, 539–542 (2011).

Du, S., Guo, F., Zank, G. P., Li, X., and Stanier, A., "Plasma energization in colliding magnetic flux ropes," Astrophys. J. **867**, 16 (2018).

Egedal, J., Daughton, W., and Le, A., "Large-scale electron acceleration by parallel electric fields during magnetic reconnection," Nat. Phys. **8**, 321–324 (2012).

Egedal, J., Fox, W., Katz, N., Porkolab, M., Øieroset, M., Lin, R. P., Daughton, W., and Drake, J. F., "Evidence and theory for trapped electrons in guide field magnetotail reconnection," J. Geophys. Res.: Space Phys. **113**, A12207, https://doi.org/10.1029/2008JA013520 (2008).

Eriksson, S., Lapenta, G., Newman, D. L., Phan, T. D., Gosling, J. T., Lavraud, B., Khotyaintsev, Y. V., Carr, C. M., Markidis, S., and Goldman, M. V., "On multiple reconnection X-lines and tripolar perturbations of strong guide magnetic fields," Astrophys. J. **805**, 43 (2015).

Eriksson, S., Newman, D. L., Lapenta, G., and Angelopoulos, V., "On the signatures of magnetic islands and multiple x-lines in the solar wind as observed by ARTEMIS and WIND," Plasma Phys. Controlled Fusion **56**, 064008 (2014).

Eriksson, S., Swisdak, M., Weygand, J. M., Mallet, A., Newman, D. L., Lapenta, G., Wilson, L. B. III, Turner, D. L., and Larsen, B., "Characteristics of multiscale current sheets in the solar wind at 1 AU associated with magnetic reconnection and the case for a heliospheric current sheet avalanche," Astrophys. J. **933**, 131 (2022).

Furno, I., Intrator, T. P., Hemsing, E. W., Hsu, S. C., Abbate, S., Ricci, P., and Lapenta, G., "Coalescence of two magnetic flux ropes via collisional magnetic reconnection," Phys. Plasmas **12**, 055702 (2005).

Gosling, J. T., "Magnetic reconnection in the solar wind," Space Sci. Rev. **172**, 187–200 (2012).

Gosling, J. T. and Phan, T. D., "Magnetic reconnection in the solar wind at current sheets with extremely small field shear angles," Astrophys. J. **763**, L39 (2013).

Haggerty, C. C., Shay, M. A., Drake, J. F., Phan, T. D., and McHugh, C. T., "The competition of electron and ion heating during magnetic reconnection," Geophys. Res. Lett. **42**, 9657–9665, https://doi.org/10.1002/2015GL065961 (2015).
Huang, C., Lu, Q., Zhang, H., Wu, M., Dong, Q., Lu, S., and Wang, S., "Kinetic simulations of the structures of magnetic island in multiple x line guide field reconnection," Phys. Plasmas **19**, 042111 (2012).
Khabarova, O., Zank, G. P., Li, G., le Roux, J. A., Webb, G. M., Dosch, A., and Malandraki, O. E., "Small-scale magnetic islands in the solar wind and their role in particle acceleration. I. Dynamics of magnetic islands near the heliospheric current sheet," Astrophys. J. **808**, 181 (2015).
Klein, K. G. and Vech, D., "Solar wind plasma parameter distributions at 1 AU," Res. Notes AAS **3**, 107 (2019).
Lapenta, G., "Particle simulations of space weather," J. Comput. Phys. **231**, 795 (2012).
Lapenta, G., Brackbill, J. U., and Ricci, P., "Kinetic approach to microscopic-macroscopic coupling in space and laboratory plasmas," Phys. Plasmas **13**, 055904 (2006).
Loureiro, N. F. and Uzdensky, D. A., "Magnetic reconnection: From the Sweet–Parker model to stochastic plasmoid chains," Plasma Phys. Controlled Fusion **58**, 014021 (2016).
Malaspina, D. M., Newman, D. L., Willson, L. B. III, Goetz, K., Kellogg, P. J., and Kerstin, K., "Electrostatic solitary waves in the solar wind: Evidence for instability at solar wind current sheets," J. Geophys. Res.: Space Phys. **118**, 591–599, https://doi.org/10.1002/jgra.50102 (2013).
Markidis, S., Henri, P., Lapenta, G., Divin, A., Goldman, M., Newman, D., and Laure, E., "Kinetic simulations of plasmoid chain dynamics," Phys. Plasmas **20**, 082105 (2013).
Markidis, S., Lapenta, G., and Uddin, R., "Multi-scale simulations of plasma with iPIC3D," Math. Comput. Simul. **80**, 1509 (2010).
MATLAB version 9.11.0 (R2021b), The MathWorks, Inc., Natick, MA, 2021.
Neukirch, T., Vasko, I. Y., Artemyev, A. V., and Allanson, O., "Kinetic models of tangential discontinuities in the solar wind," Astrophys. J. **891**, 86 (2020).
Oka, M., Phan, T.-D., Krucker, S., Fujimoto, M., and Shinohara, I., "Electron acceleration by multi-island coalescence," Astrophys. J. **714**, 915–926 (2010).
Parker, E. N., "Sweet's mechanism for merging magnetic fields in conducting fluids," J. Geophys. Res. (1896-1977) **62**, 509–520, https://doi.org/10.1029/JZ062i004p00509 (1957).
Pongkitiwanichakul, P., Ruffolo, D., Guo, F., Du, S., Suetrong, P., Yannawa, C., Makwana, K., and Malakit, K., "Role of parallel solenoidal electric field on energy conversion in 2.5d decaying turbulence with a guide magnetic field," Astrophys. J. **923**, 182 (2021).
Ricci, P., Brackbill, J. U., Daughton, W., and Lapenta, G., "Collisionless magnetic reconnection in the presence of a guide field," Phys. Plasmas **11**, 4102–4114 (2004).
Sauppe, J. P. and Daughton, W., "Kinetic-scale flux rope reconnection in periodic and line-tied geometries," Phys. Plasmas **25**, 012901 (2018).
Smith, E. J., "The heliospheric current sheet," J. Geophys. Res.: Space Phys. **106**, 15819–15831, https://doi.org/10.1029/2000JA000120 (2001).
Sweet, P. A., "The neutral point theory of solar flares," in *Proceedings of the IAU Symposium 6 on Electromagnetic Phenomena in Cosmical Physics*, edited by B. Lehnert (Cambridge University Press, Cambridge, 1958), p. 123.
Swisdak, M., Opher, M., Drake, J. F., and Bibi, F. A., "The vector direction of the interstellar magnetic field outside the heliosphere," Astrophys. J. **710**, 1769–1775 (2010).
Swisdak, M., Rogers, B. N., Drake, J. F., and Shay, M. A., "Diamagnetic suppression of component magnetic reconnection at the magnetopause," J. Geophys. Res.: Space Phys. **108**, 1218, https://doi.org/10.1029/2002JA009726 (2003).
Tsurutani, B., Lakhina, G., Verkhoglyadova, O., Gonzalez, W., Echer, E., and Guarnieri, F., "A review of interplanetary discontinuities and their geomagnetic effects," J. Atmos. Sol.-Terr. Phys. **73**, 5–19 (2011).
Uzdensky, D. A. and Loureiro, N. F., "Magnetic reconnection onset via disruption of a forming current sheet by the tearing instability," Phys. Rev. Lett. **116**, 105003 (2016).
Vasko, I. Y., Alimov, K., Phan, T., Bale, S. D., Mozer, F. S., and Artemyev, A. V., "Kinetic-scale current sheets in the solar wind at 1 AU: Scale-dependent properties and critical current density," Astrophys. J. Lett. **926**, L19 (2022).
Vasko, I. Y., Alimov, K., Phan, T. D., Bale, S. D., Mozer, F. S., and Artemyev, A. V., "Kinetic-scale current sheets in the solar wind at 1 AU: Properties and the necessary condition for reconnection," Astrophys. J. Lett. **923**, L19 (2021).
Wilson, F., Neukirch, T., and Allanson, O., "Collisionless distribution functions for force-free current sheets: Using a pressure transformation to lower the plasma beta," J. Plasma Phys. **84**, 905840309 (2018).
Wilson, L. B. III, Brosius, A. L., Gopalswamy, N., Nieves-Chinchilla, T., Szabo, A., Hurley, K., Phan, T., Kasper, J. C., Lugaz, N., Richardson, I. G., Chen, C. H. K., Verscharen, D., Wicks, R. T., and TenBarge, J. M., "A quarter century of wind spacecraft discoveries," Rev. Geophys. **59**, e2020RG000714, https://doi.org/10.1029/2020RG000714 (2021).
Zank, G. P., Hunana, P., Mostafavi, P., Roux, J. A. L., Li, G., Webb, G. M., Khabarova, O., Cummings, A., Stone, E., and Decker, R., "Diffusive shock acceleration and reconnection acceleration processes," Astrophys. J. **814**, 137 (2015).
Zank, G. P., le Roux, J. A., Webb, G. M., Dosch, A., and Khabarova, O., "Particle acceleration via reconnection processes in the supersonic solar wind," Astrophys. J. **797**, 28 (2014).
Zhou, Z., Xu, X., Zuo, P., Wang, Y., Xu, Q., Ye, Y., Wang, J., Wang, M., Chang, Q., Wang, X., and Luo, L., "Evidence for plasma heating at thin current sheets in the solar wind," Astrophys. J. Lett. **924**, L22 (2022).